University of Reading

School of Mathematical and Physical Sciences

Light scattering by penetrable convex polygons

Samuel Groth

August 2011

This dissertation is for a joint MSc in the Departments of Mathematics & Meteorology and is submitted in partial fulfilment of the requirements for the degree of Master of Science.

Abstract

This thesis concerns the problem of time-harmonic electromagnetic scattering by a penetrable two-dimensional convex polygon. This problem finds applications in many areas such as radar imaging, telecommunications and, of specific interest in this study, the scattering properties of atmospheric ice crystals. Standard numerical methods for such problems have a computational cost which grows linearly with the frequency of the incident wave. High frequency asymptotic approaches such as ray tracing do not suffer from this problem, however give poor accuracy at low frequencies. This thesis analyses the behaviour of optical diffraction to further the progress toward producing an approximation method for this problem which is applicable at all frequencies of the incident wave. A ray tracing algorithm is presented and the approximation produced is subtracted from that of a standard boundary element method. This difference is identified as being due to diffraction and is experimented with in order to describe some of the effects of this phenomenon in the transmission problem.

Acknowledgements

I would like to thank my supervisors Dr. Stephen Langdon and Dr. David Hewett for their help, encouragement and direction throughout this project. I would also like to thank the Natural Environmental Research Council for their financial support which allowed me to take part in this course.

Declaration

I confirm that this is my own work and the use of all material from other sources has been properly and fully acknowledged.

Signed.....

Contents

List of Figures

Chapter 1

Introduction

In this thesis we study the scattering of time-harmonic electromagnetic waves in two dimensions by a penetrable convex polygon. In particular, we focus on the problem of light scattered by a 2D ice crystal. We specify that the crystal shape must be convex, i.e. all exterior angles greater than 180°, so that the scattered light is not re-reflected by the external boundary at any point. Of course, since the crystal is penetrable (transparent), the light will be transmitted into the interior and undergo infinitely many internal reflections. At each of these reflections part of the wave's energy is reflected back into the crystal and the rest is transmitted out (except for the case of total internal reflection where all the wave's energy is reflected). Each time part of the wave's energy is transmitted out of the crystal, this contributes to the exterior 'scattered' electromagnetic field. The aim of the scattering problem is to determine this scattered field which, when combined with the incident electromagnetic field, gives us the pattern of light outside the crystal.

Since no analytic solution for scattering by a penetrable polygon exists, we must turn to numerical methods to provide an accurate approximation. Some of the standard approaches are boundary and finite element methods in which the scattered field is approximated using piecewise polynomials [6]. Figure 1.1 shows one wavelength ap-

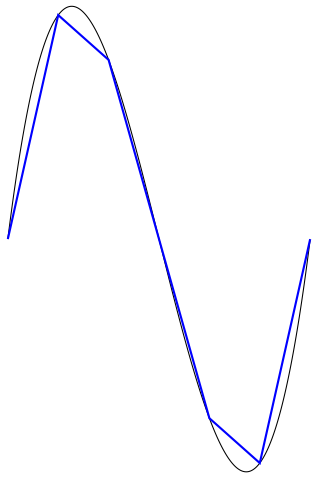

Figure 1.1: Wave approximated by piecewise polynomials. Here the polynomials are linear for clarity, however they may also be quadratic, cubic, etc.

proximated by several polynomials of degree 1. In general we may use polynomials of degree n, i.e. of the form $p = a_0 + a_1x + a_2x^2 + ... + a_nx^n$, and we say each polynomial has $(n + 1)$ degrees of freedom. So, for example, using 5 polynomials of degree 1 to approximate a wavelength is equivalent to using 2 polynomials of degree 4 (from a computational cost point of view), since they both result in 10 degrees of freedom. In order to resolve the wave solution well we must take a fixed number of degrees of freedom P for each wavelength, with the standard practice in the literature being to take $P = 10$ (see e.g. [6] or [15]). Naturally, if we shorten the wavelength of the incident light, there are more wavelengths that will fit across our scatterer, hence the number of degrees of freedom of the problem increases. The same is also true if we keep the wavelength fixed but increase the size of the scatterer.

To consider this more precisely, let D be the diameter of the smallest circle that will enclose the ice crystal and write $k = 2\pi/\lambda$ where λ is the wavelength, so that k is the wavenumber. Then the total number of degrees of freedom d required to represent the solution well on the boundary is proportional to kD. This means that these standard numerical methods become very computationally demanding for light of high frequencies (large k) or for large scatterers. Before going further, let us introduce

a quantity called the scale parameter defined as $X = kD/2\pi = D/\lambda$; this represents the number of wavelengths that fit across the diameter of the crystal. Then we can say that $d \propto X$ for these numerical methods.

Now, there are alternative methods for solving this problem whose efficiency does not scale with X. One of these, namely 'ray tracing', is the main topic of this thesis. Ray tracing is an approach which tracks the beams of light as they are reflected around inside the crystal (see Figure 1.2). This technique is purely geometrical in that it calculates the beams' reflected and transmitted directions and amplitudes based on the geometry of the shape and the direction of the incident light. If we consider enough reflections and transmissions, we can build up a representation of the scattered electromagnetic field. Since this method is geometrical, its computational cost is independent of the size parameter X. So what's wrong with it?

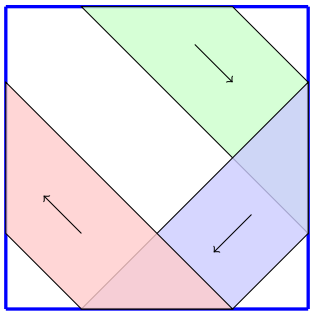

Figure 1.2: Ray tracing inside the polygon. Note that the transmitted rays have not been included in this diagram.

The drawback of ray tracing is that it is an asymptotic method, which is valid only in the limit as $X \to \infty$. From a mathematical point of view, this means that for a fixed X we cannot achieve arbitrary accuracy using a ray tracing method. From a physical point of view, the main deficiency of the method is that, in its simplest form, it does not account for the phenomenon of light 'bending' around corners, i.e. *optical diffraction*, a basic depiction of which is shown in Figure 1.3. We note here that higher-order ray tracing methods which take into account diffraction effects have been developed (e.g. the

Geometric Theory of Diffraction [13]). However, their application to the transmission problem has been limited due to the difficulty encountered in analysing the relevant 'canonical' scattering problems, such as the diffraction of a plane wave by an infinite penetrable wedge (see [16]).

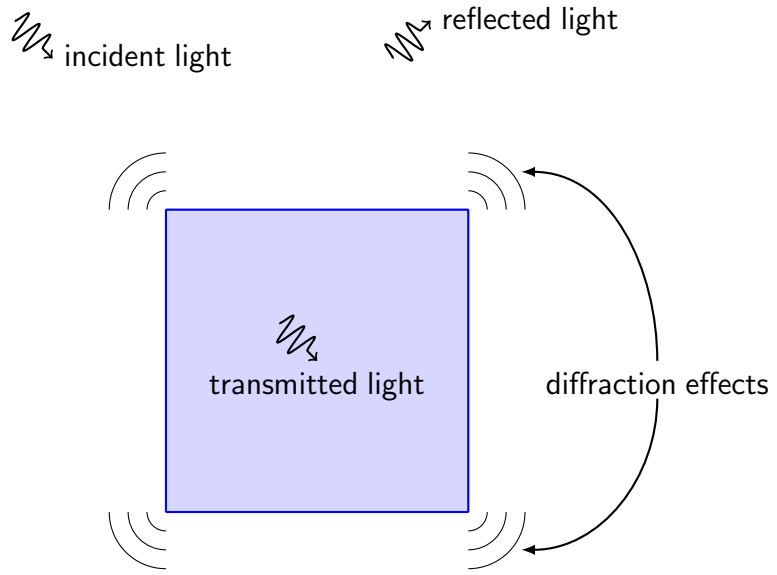

Figure 1.3: Reflection, transmission and diffraction of light.

The effect of diffraction is expected to be negligible for large X, but for small or moderate X it may be significant. In this thesis our aim is to examine the difference between the approximations obtained using a boundary element method (BEM) and a ray tracing algorithm (RTA) in order to better understand the behaviour of the diffracted field in the transmission problem. The ultimate goal of this work would be to develop a technique in which a RTA is used to evaluate the leading order behaviour (i.e. main features) of the scattered field and then a specially designed BEM is employed to efficiently evaluate the additional field due to diffraction.

Now to give a brief outline of this thesis: we begin in Chapter 2 by mentioning an important application of light scattering by ice crystals to atmospheric science and by discussing other work in the field. Chapter 3 contains an exposition of the relevant areas

in electromagnetism and the derivation of our fundamental governing equation, namely the Helmholtz equation. It is shown that solving the scalar case - which is equivalent to an acoustic transmission problem - is sufficient. Then, in Chapter 4, we reformulate the Helmholtz equation as a boundary integral equation with the aid of Green's Representation Theorem which sets us up to describe boundary element methods for solving the scattering problem numerically. Chapter 5 describes the construction of a RTA including the derivations of important geometrical equations such as Snell's Law and the Fresnel equations.

We now come to the results section of the thesis. In Chapter 6 we compare the approximations given by a RTA, written by myself, and a BEM provided by David Hewett. We also examine the convergence behaviour of the ray tracing solution. We conclude in Chapter 7 with an overview of the theory and results of the thesis and also discuss possible future directions for progress.

Chapter 2

Background and Motivation

Scattering theory attempts to understand how the propagation of acoustic and electromagnetic waves is affected by obstacles and inhomogeneities. Areas in which this theory finds applications include modelling radar, sonar, medical imaging and atmospheric particle scattering. The last example in this list is of particular interest in this thesis, but more specifically we are interested in understanding the electromagnetic scattering properties of ice crystals found in the upper atmosphere.

Most of these ice crystals are found in cirrus clouds which generally form at altitudes greater than 6 km and can permanently cover up to 30% of the Earth's surface [3]. As a consequence, these clouds have a large influence on the Earth's radiation budget and as such are an important factor to consider when predicting climate change. At present the effect of cirrus clouds on the Earth's climate is poorly understood due to the difficulty in determining their reflection and transmission properties. Knowledge of these properties would enable us to infer the *optical thickness* of cirrus clouds.

Optical thickness is a measure of transparency and tells us how much incident solar radiation is transmitted through the cloud. If a cloud is optically thin, then a large amount of the incident sunlight will be transmitted (hence a small amount will be reflected back to space) and long-wave radiation emitted from the Earth will be

absorbed which leads to a warming at the Earth's surface. If, however, a cloud is optically thick, a larger amount of incident sunlight is reflected back into space than is transmitted towards the Earth, which leads to a cooling at the surface (for further details see [2]).

The difficulty in understanding the scattering properties of these clouds stems from the fact that the constituent ice-crystals are mostly non-spherical, since no analytic solution exists for such shapes. In fact, it has been observed from aircraft and satellite observations that the ice crystals come in a large array of shapes such as hexagonal columns and plates, bullet-rosettes and hexagonal aggregates, the size of which can range from 1μm to 1000μm [11]. So the size parameter X can between 1 and 2500 for visible light, which has a wavelength λ in the range 390 nm to 750 nm.

A great deal of work has been done (see e.g. [18] and [19]) on tackling the problem of light scattering by atmospheric ice crystals and indeed a large amount of success has been achieved. However, at present there exist separate groups of techniques which are applicable for different ranges of X. As can be seen in Figure 2.1, numerical methods such as boundary and finite element methods and finite difference time domain methods are only useful for relatively small X due to computational constraints, whereas geometrical optics methods such as ray tracing are accurate for large X. There is a void between these two ranges of X for which neither approach is of use.

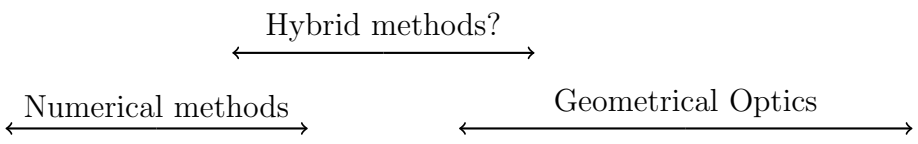

Figure 2.1: Range of ice crystal sizes over which different methods are applicable.

The prime motivation for this thesis is the desire to 'bridge this gap' by designing a method which is suitable for the values of X which currently cannot be modelled satisfactorily. We would also like this method to be 'error controllable' which means

that we would be able to obtain as accurate an approximation as we wished, for example by increasing the resolution of the mesh or by taking more terms in the series. Such a feature is present in numerical methods, however geometrical optics techniques do not have this advantage since they are fundamentally an asymptotic approximation and so will never resolve the effects of diffraction.

Another motivation for this work is the goal to develop one model which can be applied for all values of X, since we wish ultimately to simulate the scattering properties of an entire cloud of ice crystals with a range of sizes. To this end, Yang and Liou have designed a novel geometric ray tracing model, to which the RTA created in this thesis is similar, which is highly accurate for large values of X but increasingly less accurate as X decreases. Also, Silveira [17] has taken the X-independent Galerkin boundary element method of Chandler-Wilde and Langdon [6], which was designed for the sound soft acoustic problem, and applied it to the transmission problem of concern here. Silveira's approach is to incorporate diffraction but ignore reflections of the rays within the interior of the obstacle. More precisely, the leading order behaviour on the sides in shadow is assumed to be negligible. The quality of the results from Silveira's study suggests that we must use a more sophisticated approach in ascertaining the leading order behaviour on the shadowed sides [17]. Note that by 'shadowed sides' we mean those which are not lit by the incident light directly, i.e. the light must pass through the crystal to hit them.

In this thesis we take the first steps to improving upon Silveira's attempt to extend the reach of numerical methods. Our approach will be to study the difference between the leading order behaviour of the field u_l and the total field u. We term this difference u_d and write it explicitly as

$$u_d = u - u_l.$$

This is done by first supposing that u_l can be determined by the RTA and that u_d is therefore due to diffraction effects. By studying u_d and understanding its properties for different size parameters and shapes (which is the aim of this project) we may

hope in future studies to further the work of Chandler-Wilde and Langdon in [6] in order to develop an X-independent numerical method for the transmission problem. This would constitute a major advance in the area of computational methods for high-frequency scattering problems. Such a method would use a RTA to calculate the leading order behaviour, u_l, and a specially designed BEM to calculate the extra field due to diffraction effects.

Chapter 3

Electromagnetism

Light waves are the manifestation of perturbations in the electromagnetic field and, as such, any attempt to understand the scattering behaviour of light must begin with an exposition of the theory of electromagnetism. We begin by stating the four fundamental equations first written down by James Clerk Maxwell in 1861 and see how they simplify when considering light travelling through air and ice. We find that we may ignore one of the five vectors of electromagnetism since it is negligibly small in these two media. In §3.2 we consider the conditions that we require the electromagnetic vectors to satisfy on the boundary of the ice crystal. It is important to enforce such conditions because Maxwell's equations are only valid for media in which certain properties such as the dielectric constant – which we see in §3.3 is analogous to the refractive index – are continuous. It is well known that light refracts or 'bends' as it passes from air into ice because their respective refractive indices are different. Therefore we must impose boundary conditions at the surface of the crystal to ensure that Maxwell's equations hold here.

In §3.3 we demonstrate that light travels as waves and, restricting our attention to time-harmonic waves, we derive our governing equation, that is Helmholtz's equation. Finally in §3.4 we look at the 2D case which is relevent in this thesis and show that we

arrive at the scalar transmission problem, which is equivalent to the 2D acoustic case.

3.1 Maxwell's Equations

In this section, and the following two, we follow the exposition of Born and Wolf [4]. The electric vector $\mathbf{E}$ and the magnetic induction $\mathbf{B}$ together constitute the electromagnetic field. To describe the effect of the field on matter we must introduce three further vectors: $\mathbf{j}$ the electric current density, $\mathbf{D}$ the electric displacement and $\mathbf{H}$ the magnetic vector. The space and time derivatives of these five vectors are related via Maxwell's equations [1]

$$\nabla \times \mathbf{H} - \frac{1}{c}\dot{\mathbf{D}} = \frac{4\pi}{c}\mathbf{j}, \tag{3.1}$$

$$\nabla \times \mathbf{E} + \frac{1}{c}\dot{\mathbf{B}} = 0, \tag{3.2}$$

$$\nabla \cdot \mathbf{D} = 4\pi\rho, \tag{3.3}$$

$$\nabla \cdot \mathbf{B} = 0, \tag{3.4}$$

where ρ is the electric charge density and c is the speed of light in a vacuum.

3.2 Material Equations and Boundary Conditions

In order to solve Maxwell's equations uniquely we require additional relations between our five vectors which describe how substances behave under the influence of the electromagnetic field. If the field is time-harmonic (see §3.3), all bodies are at rest and the materials are isotropic (i.e. uniform in all orientations and directions), then we have

[1] Here and throughout the dot denotes differentiation with respect to time, e.g. $\dot{\mathbf{B}} = \frac{\partial \mathbf{B}}{\partial t}$

the *material equations*

$$\mathbf{j} = \sigma\mathbf{E}, \tag{3.5}$$

$$\mathbf{D} = \varepsilon\mathbf{E}, \tag{3.6}$$

$$\mathbf{B} = \mu\mathbf{H}, \tag{3.7}$$

where σ is the electrical conductivity, ε is the dielectric constant and μ is the magnetic permeability. For non-magnetic, transparent substances such as ice and air, μ is equal to unity. For generality, however, we retain μ in all of the formulae in this chapter but we are mostly interested in the case $\mu = 1$. Also we have that ice and air are insulators so $\sigma \approx 0$ and hence we take $\mathbf{j} = 0$.

By combining the general Maxwell equations (3.1)–(3.4) with the material equations (3.5)–(3.7), taking $\mathbf{j} = 0$ and assuming there are no electric charges in the region concerned so that the electric charge density $\rho = 0$, we derive a set of Maxwell's equations in terms of $\mathbf{H}$ and $\mathbf{E}$ alone which are specific to the problem proposed in this thesis. These equations read

$$\nabla \times \mathbf{H} - \frac{\varepsilon}{c}\dot{\mathbf{E}} = 0, \tag{3.8}$$

$$\nabla \times \mathbf{E} + \frac{\mu}{c}\dot{\mathbf{H}} = 0, \tag{3.9}$$

$$\nabla \cdot \mathbf{H} = 0, \tag{3.10}$$

$$\nabla \cdot \mathbf{E} = 0. \tag{3.11}$$

The value for ε is assumed to be constant within each medium. However, there is a discontinuity in ε at the boundary between air and ice since it has different values in each medium. Therefore we must impose appropriate 'jump' conditions at this boundary.

The appropriate boundary conditions can be found by replacing the plane of discontinuity (i.e. the interface between air and ice) with a thin layer in which ε varies quickly but continuously between the two media, and then taking limits as the boundary is approached (see Chapter 1, page 3 of [4] for more details). The results of this

procedure are the conditions

$$\mathbf{n} \cdot [\mu \mathbf{H}] = 0, \tag{3.12}$$

$$\mathbf{n} \cdot [\varepsilon \mathbf{E}] = 0, \tag{3.13}$$

$$\mathbf{n} \times [\mathbf{H}] = 0, \tag{3.14}$$

$$\mathbf{n} \times [\mathbf{E}] = 0, \tag{3.15}$$

where $[\cdot]$ represents the jump of a quantity across the interface. Physically, (3.12)–(3.13) state that the normal components of both $\mu\mathbf{H}$ and $\varepsilon\mathbf{E}$ must be continuous across the boundary. Conditions (3.14)–(3.15) say that the tangential components of $\mathbf{H}$ and $\mathbf{E}$ must also be continuous across the boundary.

3.3 The Wave and Helmholtz Equations

Using equations (3.8)–(3.11) we may now show that electromagnetic radiation (rather reassuringly) propagates in the form of a wave. This is done by deriving the wave equation for both the electric vector $\mathbf{E}$ and the magnetic vector $\mathbf{H}$.

Firstly we take the curl of (3.9)

$$\nabla \times (\nabla \times \mathbf{E}) + \frac{\mu}{c} \nabla \times \dot{\mathbf{H}} = 0, \tag{3.16}$$

and differentiate (3.8) with respect to time to obtain

$$\nabla \times \dot{\mathbf{H}} - \frac{\varepsilon}{c} \ddot{\mathbf{E}} = 0. \tag{3.17}$$

Subtracting (3.17) from (3.16) and applying the identity[2]

$$\text{curl curl} \equiv \text{grad div} - \Delta \tag{3.18}$$

gives

$$\nabla(\nabla \cdot \mathbf{E}) - \Delta \mathbf{E} + \frac{\varepsilon \mu}{c^2} \ddot{\mathbf{E}} = 0. \tag{3.19}$$

[2]Throughout this thesis we use the notation that $\Delta = \nabla^2$.

From (3.11) we know that $\nabla \cdot \mathbf{E} = 0$, hence we have

$$\Delta \mathbf{E} - \frac{\varepsilon\mu}{c^2}\ddot{\mathbf{E}} = 0, \tag{3.20}$$

which is known as the *wave equation*. Using similar steps, but instead with equations (3.9) and (3.8) switched, it is easy to arrive at the wave equation for $\mathbf{H}$

$$\Delta \mathbf{H} - \frac{\varepsilon\mu}{c^2}\ddot{\mathbf{H}} = 0. \tag{3.21}$$

Together these two equations suggest that electromagnetic radiation propagates through ice and air as waves with velocity

$$v = \frac{c}{\sqrt{\varepsilon\mu}}, \tag{3.22}$$

where $\sqrt{\varepsilon\mu} =: m$ is the refractive index of the medium and c is the speed of light in a vacuum. In this study we have taken values for the two refractive indices, m_1 and m_2 to be

$$m_1 = 1, \quad \text{in air}, \tag{3.23}$$

$$m_2 = 1.31, \quad \text{in ice}. \tag{3.24}$$

Equation (3.22) tells us that light travels slower through media with a larger refractive index. This implies that as light passes from air into the ice it will slow down and hence be refracted towards the normal to the boundary, and as the light passes out of the crystal it will speed up and hence be refracted away from the normal. The details of this refraction process are discussed further in Chapter 5.

Now we further specialise our formulae by considering the time-harmonic case, namely when the electric and magnetic fields are of the form

$$\mathbf{E}(\mathbf{x}, \mathbf{t}) = \mathrm{Re}\left\{\mathbf{E_0}(\mathbf{x})e^{-\mathrm{i}\omega t}\right\}, \quad \mathbf{H}(\mathbf{x}, \mathbf{t}) = \mathrm{Re}\left\{\mathbf{H_0}(\mathbf{x})e^{-\mathrm{i}\omega t}\right\}, \tag{3.25}$$

where ω is the phase. In this case the electric and magnetic fields are oscillating with the same period but with different directions determined by the vectors $\mathbf{E_0}(\mathbf{x})$ and

$\mathbf{H_0}(\mathbf{x})$ respectively. By substituting (3.25) into the Maxwell equations (3.8)–(3.11), the *Time-Harmonic Maxwell equations* arise

$$\nabla \times \mathbf{H_0} + \frac{\mathrm{i}\omega\varepsilon}{c}\mathbf{E_0} = 0, \tag{3.26}$$

$$\nabla \times \mathbf{E_0} - \frac{\mathrm{i}\omega\mu}{c}\mathbf{H_0} = 0, \tag{3.27}$$

$$\nabla \cdot \mathbf{H_0} = 0, \tag{3.28}$$

$$\nabla \cdot \mathbf{E_0} = 0. \tag{3.29}$$

Taking the curl of (3.26) and (3.27) and using the identity (3.18) gives us

$$\nabla(\nabla \cdot \mathbf{H_0}) - \Delta\mathbf{H_0} + \frac{\mathrm{i}\omega\varepsilon}{c}(\nabla \times \mathbf{E_0}) = 0, \tag{3.30}$$

then using the relations (3.27) and (3.28) we obtain the *Helmholtz equation* for $\mathbf{H_0}$,

$$\left(\Delta + k^2\right)\mathbf{H_0} = 0, \tag{3.31}$$

where k is the wavenumber defined as

$$k^2 = \frac{\omega^2\varepsilon}{c^2}. \tag{3.32}$$

Similarly the Helmholtz equation may be derived for $\mathbf{E_0}$,

$$\left(\nabla^2 + k^2\right)\mathbf{E_0} = 0. \tag{3.33}$$

Of course, (3.31) and (3.33) could equivalently have been obtained by substituting (3.25) into (3.21) and (3.20).

3.4 The 2D case

In this thesis we are concerned with time-harmonic scattering by a two-dimensional penetrable obstacle. In this section we shall reduce the dependence of the electric and magnetic fields by one dimension, and show that, in this case, the electromagnetic scattering problem is equivalent to a scalar (or *acoustic*) transmission problem.

We begin by assuming that the vectors $\mathbf{E_0}$ and $\mathbf{H_0}$ have no z-dependence, i.e. $\mathbf{E_0} = \mathbf{E_0}(x, y)$ and $\mathbf{H_0} = \mathbf{H_0}(x, y)$, although they may have z-components. It is convenient to introduce the notation

$$\mathbf{E}_\perp := (0, 0, E_z), \tag{3.34}$$

$$\mathbf{E}_\parallel := (E_x, E_y, 0), \tag{3.35}$$

$$\mathbf{H}_\perp := (0, 0, H_z), \tag{3.36}$$

$$\mathbf{H}_\parallel := (H_x, H_y, 0), \tag{3.37}$$

where $\mathbf{E_0} = (E_x, E_y, E_z)$ and $\mathbf{H_0} = (H_x, H_y, H_z)$ so that $\mathbf{E_0} = \mathbf{E}_\perp + \mathbf{E}_\parallel$ and $\mathbf{H_0} = \mathbf{H}_\perp + \mathbf{H}_\parallel$.

The first two spatial components of (3.26) give us

$$\frac{\partial H_z}{\partial y} = -\frac{\mathrm{i}\omega\varepsilon}{c} E_x, \tag{3.38}$$

$$\frac{\partial H_z}{\partial x} = \frac{\mathrm{i}\omega\varepsilon}{c} E_y. \tag{3.39}$$

Hence it is only necessary to solve for $\mathbf{H}_\perp$ (i.e. H_z) in order to find $\mathbf{E}_\parallel$. Similarly, the first two spacial components of (3.27) give

$$\frac{\partial E_z}{\partial y} = \frac{\mathrm{i}\omega\mu}{c} H_x, \tag{3.40}$$

$$\frac{\partial E_z}{\partial x} = -\frac{\mathrm{i}\omega\mu}{c} H_y. \tag{3.41}$$

So knowledge of $\mathbf{E}_\perp$ (i.e. E_z) allows us to determine $\mathbf{H}_\parallel$. Now we wish to show that from the conditions (3.12)–(3.15) and using the relations (3.38)–(3.41), scalar boundary conditions for E_z and H_z may be obtained.

For the electric field $\mathbf{E} = (E_x, E_y, E_z)$, the component in the plane tangential to $\mathbf{n}$ is $-(\mathbf{E} \times \mathbf{n}) \times \mathbf{n}$. So the conditon (3.15), $\mathbf{n} \times [\mathbf{E}] = 0$, means that the tangential component of $\mathbf{E}$ is continuous across the boundary, in particular

$$[\mathbf{E}_\perp] = 0, \quad \text{i.e.} \quad [E_z] = 0, \tag{3.42}$$

which is the first of our derived boundary conditions. Similarly, (3.14) implies that

$$[\mathbf{H}_\perp] = 0, \quad \text{i.e.} \quad [H_z] = 0, \tag{3.43}$$

We also have by the linearity of the curl operator that

$$\mathbf{n} \times [\mathbf{E}] = \underbrace{\mathbf{n} \times \left[\mathbf{E}_\parallel\right]}_{x,y\text{-plane}} + \underbrace{\mathbf{n} \times [\mathbf{E}_\perp]}_{z\text{-plane}}. \tag{3.44}$$

Since the first component lives in the (x, y)-plane and the second in the z-plane, they are orthogonal, hence we must have that

$$\mathbf{n} \times \left[\mathbf{E}_\parallel\right] = 0, \tag{3.45}$$

and

$$\mathbf{n} \times [\mathbf{E}_\perp] = 0. \tag{3.46}$$

Now, if $\mathbf{n} \neq 0$ and $\mathbf{E}_\parallel \neq 0$ both lie in the same plane and $\mathbf{n} \times \mathbf{E}_\parallel = 0$, then $\mathbf{E}_\parallel = \alpha \mathbf{n}$ for some $\alpha \in \mathbb{C}$, hence we may deduce that

$$\mathbf{t} \cdot \mathbf{E} = 0,$$

where $\mathbf{t} = (-n_2, n_1)$ is perpendicular to the normal $\mathbf{n} = (n_1, n_2)$. This implies that

$$n_1 E_y = n_2 E_x. \tag{3.47}$$

Hence we see that the boundary condition (3.15), $\mathbf{n} \times [\mathbf{E}] = 0$, also implies that

$$\left[\frac{1}{\varepsilon} \frac{\partial H_z}{\partial n}\right] = 0. \tag{3.48}$$

Similarly, one can show that

$$\left[\frac{1}{\mu} \frac{\partial E_z}{\partial n}\right] = 0. \tag{3.49}$$

The 2D electromagnetic scattering problem is therefore equivalent to solving two scalar Helmholtz equations

$$\left(\Delta + k^2\right) E_z = 0, \tag{3.50}$$

$$\left(\Delta + k^2\right) H_z = 0, \tag{3.51}$$

subject to the boundary conditions

$$[H_z] = 0, \tag{3.52}$$

$$[E_z] = 0, \tag{3.53}$$

$$\left[\frac{1}{\varepsilon}\frac{\partial H_n}{\partial n}\right] = 0, \tag{3.54}$$

$$\left[\frac{1}{\mu}\frac{\partial E_z}{\partial n}\right] = 0. \tag{3.55}$$

We will from here onwards consider only one of the fields, say E_z, and denote this quantity in accordance with much of the literature as $u(\mathbf{x})$. Our problem to solve is therefore

$$\left(\Delta + k^2\right) u = 0, \tag{3.56}$$

where u is subject to the following conditions on the air-ice interface:

$$[u] = 0, \tag{3.57}$$

$$\left[\alpha\frac{\partial u}{\partial n}\right] = 0. \tag{3.58}$$

For ease of presentation we restrict our attention to the case $\alpha = 1$ in what follows, but generalising to $\alpha \neq 1$ would be straightforward.

Chapter 4

Boundary Integral Formulation

Chapter 3 culminated in setting down the mathematical formulation of the problem we wish to solve. The focus of this chapter is solving it. In particular, we begin in §4.1 by establishing the notation to be used and by restating the problem more precisely.

In §4.2 a remarkable mathematical tool, Green's representation theorem, is employed to reformulate the 2D scattering problem as an integral equation over the boundary of the obstacle. This operation allows us to compute the solution in the entire domain, i.e. throughout both the regions of air and ice of interest, only from knowledge of the information on the boundary of the obstacle; effectively reducing the dimension of the problem from two to one.

Lastly, in §4.3 a brief description of a boundary element method is given. BEMs are one class of numerical methods for solving scattering problems, the limitations of which were discussed in Chapter 1. The following Chapter 5 will discuss in detail an alternative approach, namely ray tracing, which is the main focus of this thesis.

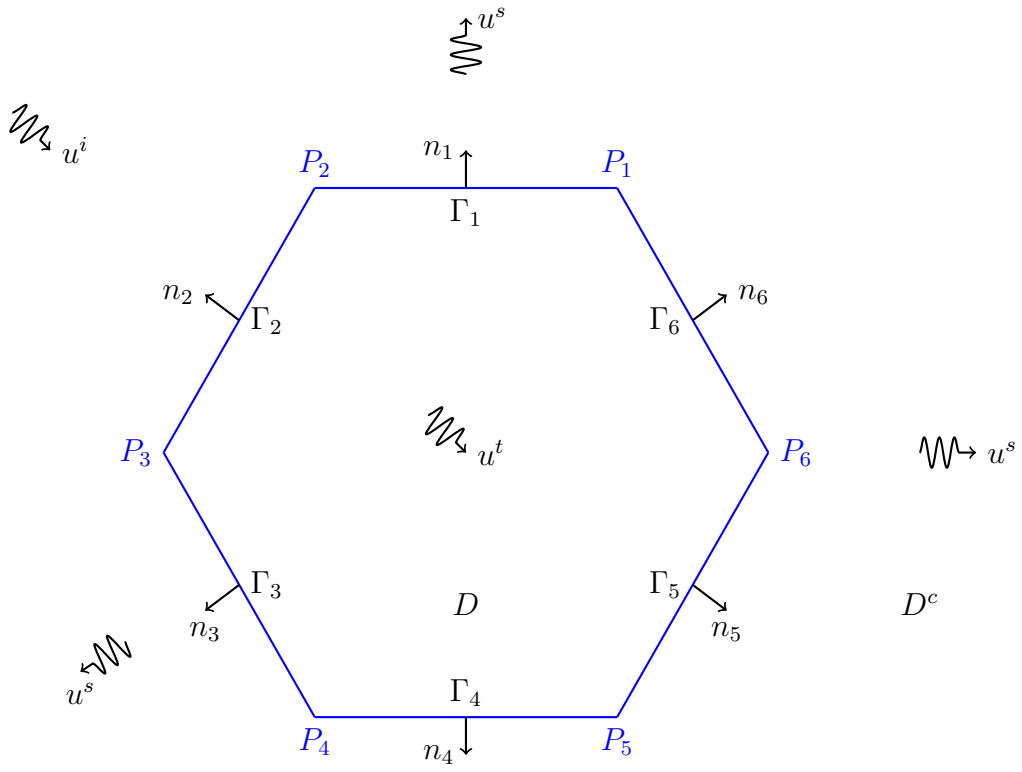

Figure 4.1: Polygon notation.

4.1 The Setup

The notational setup can be seen in Figure 4.1. The notation is defined formally as follows. Let D denote the bounded open domain within the convex polygon and $D^c := \mathbb{R}^2 \setminus \overline{D}$ be the unbounded exterior domain. The boundary of D is $\Gamma := \cup_{i=1}^{n} \Gamma_i$, where Γ_i, $i = 1, \ldots, n$, are the n sides of the polygon. The incident plane wave u^i is directed from the top left of the figure towards the polygonal scatterer. Once this wave strikes Γ, it is partially reflected back into D^c and partially transmitted into D. The scattered field u^s comprises this initially reflected light as well as that which is transmitted into the shape, and then out again. We refer to the field in D by u^t, so

$$u = u^t, \qquad \text{in } D,$$

where u^t is the 'transmitted' field and denote the field outside the scatterer (in D^c) by u, so

$$u = u^s + u^i, \qquad \text{in } D^c.$$

The scattered light u^s and the transmitted light u^t both satisfy the Helmholtz equation, i.e.

$$(\Delta + k_1)\, u^s = 0 \qquad \text{in } D^c, \tag{4.1}$$

$$(\Delta + k_2)\, u^t = 0 \qquad \text{in } D, \tag{4.2}$$

where k_1 and k_2 are the wavenumbers for u^s and u^t respectively. Their ratio is equal to that of the refractive indices m_1 and m_2, i.e.

$$\frac{k_1}{k_2} = \frac{m_1}{m_2}.$$

Equations (4.1)–(4.2) are supplemented by the boundary conditions

$$[u] = 0 \qquad \text{on } \Gamma, \tag{4.3}$$

$$\left[\frac{\partial u}{\partial n}\right] = 0 \qquad \text{on } \Gamma, \tag{4.4}$$

where n is the normal to Γ pointing into D^c. We also require for uniqueness that the scattered field u^s satisfies the *Sommerfeld radiation conditions*,

$$u^s(\mathbf{x}) = O\left(r^{-1/2}\right), \tag{4.5}$$

$$\frac{\partial u^s}{\partial r}(\mathbf{x}) - iku^s(\mathbf{x}) = o\left(r^{-1/2}\right), \tag{4.6}$$

as $r \to \infty$ where $r = |\mathbf{x}|$, and the limit holds uniformly in all directions. In fact, we need only state the second condition since it can be shown that the first follows on from the second. However, it is useful to consider both to assist the physical interpretation. The first condition means that $|u|^2$ decreases in proportion to $1/r$ as r goes to infinity. Considered physically, this seems perfectly reasonable since as the light radiates outward from its source, the energy of the light (which is proportional to $|u|^2$) is spread over a circle of ever increasing circumference $2\pi r$. The second condition translates as

saying that far away from the scatterer the light wave appears locally like a plane wave travelling in the direction of increasing r (i.e. outward from the source) [5].

Existence and uniqueness of the solution to the transmission problem can be proved under certain assumptions made on the wavenumbers k_1 and k_2, as detailed in [8], p.386. We highlight one sufficient condition from [8] for existence and uniqueness which is of relevence to our particular setup, which is that we require

$$k_1 > 0 \quad \text{and} \quad k_2 > 0. \tag{4.7}$$

Throughout we take $k_1 = 1$ and $k_2 = 1.31$, so we can be assured that our problem has a unique solution.

4.2 Integral Equation Formulation

In this section we employ the so called *direct method* as used by Silveira [17] (see also [7, §3.2]) to derive an integral equation formulation which reduces the number of dimensions of the problem from two to one. This is done using Green's theorems. We state these for a bounded domain V with a C^2 boundary and suppose that the functions $\phi, \psi \in C^2(V) \cap C(\overline{V})$ have normal derivatives on the boundary ∂V in the sense that the limit

$$\frac{\partial \phi(x)}{\partial n} = \lim_{h \to 0} \left(n(x), \nabla \phi(x - hn(x)) \right), \text{ for } x \in \partial V, \tag{4.8}$$

exists uniformly on ∂V, and a similar condition holds for the normal derivative of ψ. Then this suffices to ensure that Green's first theorem

$$\int_V (\phi \Delta \psi + \nabla \phi \cdot \nabla \psi) \, \mathrm{d}\mathbf{x} = \int_{\partial V} \phi \frac{\partial \psi}{\partial n}, \tag{4.9}$$

and Green's second theorem

$$\int_V (\phi \Delta \psi - \psi \Delta \phi) = \int_{\partial V} \left(\phi \frac{\partial \psi}{\partial n} - \psi \frac{\partial \phi}{\partial n} \right) \mathrm{d}s, \tag{4.10}$$

are both valid. We have stated Green's theorems for the case where V is a bounded domain with C^2 boundary and $\phi, \psi \in C^2(V) \cap C(\overline{V})$. However, we note that our

polygonal domain is a Lipschitz domain. In this case we must state Green's theorems in a slightly different manner. We will not present this statement here but refer the reader to [14] for a rigorous exposition.

Firstly we note that the fundamental solutions of the Helmholtz equations (4.1)–(4.2) are

$$\Phi_{1,2}(\mathbf{x},\mathbf{y}) = \frac{\mathrm{i}}{4} H_0^{(1)}\left(k_{1,2}|\mathbf{x}-\mathbf{y}|\right), \tag{4.11}$$

where $H_0^{(1)}(\cdot)$ is the Hankel function of the first kind of order zero (see [1] for properties of this function). Now, applying Green's second theorem (see Theorem 3.1 of [7] for details) to u^t and Φ in D, we obtain

$$\int_{\partial D}\left(u^t(y)\frac{\partial \Phi_2(x,y)}{\partial n(y)} - \Phi_2(x,y)\frac{\partial u^t(y)}{\partial n}\right)\mathrm{d}s(y) = \begin{cases} -u^t(x), & x \in D, \\ 0, & x \in D^c. \end{cases} \tag{4.12}$$

Then applying Green's first theorem as in Theorem 3.3 of [7] in D^c we arrive at

$$\int_{\partial D}\left(u^s(y)\frac{\partial \Phi_1(x,y)}{\partial n(y)} - \Phi_1(x,y)\frac{\partial u^s(y)}{\partial n}\right)\mathrm{d}s(y) = \begin{cases} 0, & x \in D, \\ u^s(x), & x \in D^c. \end{cases} \tag{4.13}$$

Combining (4.12) and (4.13) we obtain the integral representation for the transmission problem

$$u^t(x) = \int_\Gamma \left(\Phi_2(x,y)\frac{\partial u^t(y)}{\partial n} - u^t(y)\frac{\partial \Phi_2(x,y)}{\partial n(y)}\right)\mathrm{d}s(y), \quad x \in D, \tag{4.14}$$

$$u^s(x) = \int_\Gamma \left(u^s(y)\frac{\partial \Phi_1(x,y)}{\partial n(y)} - \Phi_1(x,y)\frac{\partial u^s(y)}{\partial n}\right)\mathrm{d}s(y), \quad x \in D^c. \tag{4.15}$$

Note that

$$\int_\Gamma \left(u^i(y)\frac{\partial \Phi_1(x,y)}{\partial n(y)} - \Phi_1(x,y)\frac{\partial u^i(y)}{\partial n}\right)\mathrm{d}s(y) = 0, \tag{4.16}$$

so we may then add this term and u^i to both sides of equation (4.15) to obtain an integral equation for the entire field u as opposed to merely the scattered field. This gives us

$$u(x) = \int_\Gamma \left(u(y)\frac{\partial \Phi_1(x,y)}{\partial n(y)} - \Phi_1(x,y)\frac{\partial u(y)}{\partial n}\right)\mathrm{d}s(y) + u^i(x), \quad x \in D^c. \tag{4.17}$$

Now we let $x \to \Gamma$ in equations (4.14) and (4.17) from D and D^c respectively, and utilising the jump conditions for layer potentials (see e.g. [5]), we obtain

$$u^-(x) = \int_\Gamma \left(\Phi_2(x,y) \frac{\partial u^-(y)}{\partial n} - u^-(y) \frac{\partial \Phi_2(x,y)}{\partial n(y)} \right) \mathrm{d}s(y) + \frac{1}{2} u^-(x), \tag{4.18}$$

$$u^+(x) = \int_\Gamma \left(u^+(y) \frac{\partial \Phi_1(x,y)}{\partial n(y)} - \Phi_1(x,y) \frac{\partial u^+(y)}{\partial n} \right) \mathrm{d}s(y) + \frac{1}{2} u^+(x) + u^i(x), \tag{4.19}$$

where the notation f^+ and f^- denotes the limits as $x \to \Gamma$ of any function f from D^c and D respectively. Similarly, taking the normal derivatives to equations (4.14) and (4.17) in the limit $\mathbf{x} \to \Gamma$ from both sides shows that

$$\begin{aligned} \frac{\partial u^-(x)}{\partial n} &= \int_\Gamma \frac{\partial \Phi_2(x,y)}{\partial n(x)} \frac{\partial u^-(y)}{\partial n} \mathrm{d}s(y) - \frac{\partial}{\partial n(x)} \int_\Gamma u^-(y) \frac{\partial \Phi_2(x,y)}{\partial n(y)} \mathrm{d}s(y) \\ &+ \frac{1}{2} \frac{\partial u^-(x)}{\partial n}, \quad x \in \Gamma \end{aligned} \tag{4.20}$$

$$\begin{aligned} \frac{\partial u^+(x)}{\partial n} &= \frac{\partial}{\partial n(x)} \int_\Gamma u^+(y) \frac{\partial \Phi_1(x,y)}{\partial n(y)} \mathrm{d}s(y) - \int_\Gamma \frac{\partial u^+(y)}{\partial n} \frac{\partial \Phi_1(x,y)}{\partial n(x)} \mathrm{d}s(y) \\ &+ \frac{1}{2} \frac{\partial u^+(x)}{\partial n} + \frac{\partial u^i(x)}{\partial n}, \quad x \in \Gamma \end{aligned} \tag{4.21}$$

The equations (4.18)–(4.21) may be written in a more concise form by defining the boundary integral operators S_j, K_j, K_j' and T_j for $j = 1, 2$, as

$$S_j \psi(\mathbf{x}) := \int_\Gamma \Phi_j(\mathbf{x}, \mathbf{y}) \psi(\mathbf{x}) \mathrm{d}s(\mathbf{y}), \tag{4.22}$$

$$K_j \psi(\mathbf{x}) := \int_\Gamma \frac{\partial \Phi_j(\mathbf{x}, \mathbf{y})}{\partial n(\mathbf{y})} \psi(\mathbf{y}) \mathrm{d}s(\mathbf{y}), \tag{4.23}$$

$$K_j' \psi(\mathbf{x}) := \int_\Gamma \frac{\partial \Phi_j(\mathbf{x}, \mathbf{y})}{\partial n(\mathbf{x})} \psi(\mathbf{y}) \mathrm{d}s(\mathbf{y}), \tag{4.24}$$

$$T_j \psi(\mathbf{x}) := \frac{\partial}{\partial n(x)} \int_\Gamma \frac{\partial \Phi_j(\mathbf{x}, \mathbf{y})}{\partial n(\mathbf{y})} \psi(\mathbf{y}) \mathrm{d}s(\mathbf{y}), \tag{4.25}$$

and writing the identity operator as I. Then we write the integral equations (4.18)–

(4.21) in the form

$$u^-(x) = S_2\frac{\partial u^-(x)}{\partial n} + \left(\frac{1}{2}I - K_2\right)u^-(x), \quad x \in \Gamma, \tag{4.26}$$

$$u^+(x) = \left(\frac{1}{2}I + K_1\right)u^+(x) - S_1\frac{\partial u^+(x)}{\partial n} + u^i, \quad x \in \Gamma. \tag{4.27}$$

$$\frac{\partial u^-(x)}{\partial n} = \left(\frac{1}{2}I + K_2'\right)\frac{\partial u^-(x)}{\partial n} - T_2u^-(x), \ x \in \Gamma, \tag{4.28}$$

$$\frac{\partial u^+(x)}{\partial n} = \left(\frac{1}{2}I - K_1'\right)\frac{\partial u^+(x)}{\partial n} + T_1u^+(x) + \frac{\partial u^i(x)}{\partial n}, \ x \in \Gamma. \tag{4.29}$$

It follows from considering the boundary conditions (4.3) and (4.4) that only two of the unknown quantities u^+, u^-, $\partial u^+/\partial n$ and $\partial u^-/\partial n$ are linearly independent, in fact on the boundary Γ, $u^+ = u^- = u$ and $\partial u^-/\partial n = \partial u^+/\partial n = \partial u/\partial n$. We resolve this issue by adding the first pair (4.26)+(4.27) and adding the second pair (4.28)+(4.29) and combining them with the boundary conditions (4.3)–(4.4) to give the following system of coupled boundary integral equations (and dropping $\pm$ superscripts),

$$(I + K_2 - K_1)\,u + (S_1 - S_2)\frac{\partial u}{\partial n} = u^i, \tag{4.30}$$

$$(I + K_1' - K_2')\,\frac{\partial u}{\partial n} + (T_2 - T_1)\,u = \frac{\partial u^i}{\partial n}. \tag{4.31}$$

These equations may be written in a matrix form as

$$\mathbf{A}\chi = \mathbf{f}, \tag{4.32}$$

where

$$\mathbf{A} := \begin{pmatrix} I + K_2 - K_1 & S_1 - S_2 \\ T_2 - T_1 & 1 + K_1' - K_2' \end{pmatrix}, \tag{4.33}$$

and

$$\chi := \begin{pmatrix} u \\ \frac{\partial u}{\partial n} \end{pmatrix}, \tag{4.34}$$

also

$$\mathbf{f} := \begin{pmatrix} u^i \\ \frac{\partial u^i}{\partial n} \end{pmatrix}. \tag{4.35}$$

We remark here that other formulations are possible by combining (4.26)–(4.29) in different ways, see e.g. [12]. We can now solve the system (4.32) numerically for u and $\partial u/\partial n$ on the boundary Γ and then use equations (4.14) and (4.15) to calculate the entire field in $\mathbb{R}^2$. One standard type of numerical method for solving the matrix system (4.32) is called the boundary element method.

4.3 Boundary Element Method

The boundary element method (BEM) can be seen as a finite element method (FEM) applied to a problem that has been reformulated as a boundary integral equation. In this section we will consider only the simplest BEM (as detailed in [5]) in which the boundary Γ is divided into M equally sized boundary elements, denoted by $\gamma_1, \gamma_2, ..., \gamma_M$. Along each element we approximate the solution of the boundary integral equations (4.32) by a polynomial of degree zero (i.e. a constant), so u and $\partial u/\partial n$ are approximated in each element γ_j by u_j and v_j, respectively, for $j = 1, 2, ...M$. Since $\int_\Gamma = \int_{\gamma_1} + ... + \int_{\gamma_M}$, we have the approximations

$$\begin{aligned} u^i(x) \approx \quad & u(x) + \sum_{j=1}^{M} u_j \int_{\gamma_j} \left(\frac{\partial \Phi_2(x,y)}{\partial n(y)} - \frac{\partial \Phi_1(x,y)}{\partial n(y)} \right) \mathrm{d}s(y) \\ & + \sum_{j=1}^{M} v_j \int_{\gamma_j} \left(\Phi_1(x,y) - \Phi_2(x,y) \right) \mathrm{d}s(y), \end{aligned} \tag{4.36}$$

$$\begin{aligned} \frac{\partial u^i(x)}{\partial n} \approx \quad & \frac{\partial u(x)}{\partial n} + \sum_{j=1}^{M} v_j \int_{\gamma_j} \left(\frac{\partial \Phi_1(x,y)}{\partial n(x)} - \frac{\partial \Phi(x,y)}{\partial n(x)} \right) \mathrm{d}s(y) \\ & + \sum_{j=1}^{M} u_j \left(\frac{\partial}{\partial n} \int_{\gamma_j} \frac{\partial \Phi_2(x,y)}{\partial n(y)} \mathrm{d}s(y) - \frac{\partial}{\partial n} \int_{\gamma_j} \frac{\partial \Phi_1(x,y)}{\partial n(y)} \mathrm{d}s(y) \right). \end{aligned} \tag{4.37}$$

We then use the collocation method to obtain a set of equations which determine the constants u_j and v_j. The collocation method involves choosing so called *collocation points* $\mathbf{x}_l$ which are the midpoints of the elements γ_j and requiring that (4.36) and

(4.37) hold exactly at each of these points. We therefore require that, for $k = 1, ..., M$,

$$\begin{aligned} u_k = \quad & u^i(x_k) - \sum_{j=1}^{M} u_j \int_{\gamma_j} \left(\frac{\partial \Phi_2(x_k, y)}{\partial n(y)} - \frac{\partial \Phi_1(x_k, y)}{\partial n(y)} \right) \mathrm{d}s(y) \qquad (4.38) \\ & - \sum_{j=1}^{M} v_j \int_{\gamma_j} (\Phi_1(x_k, y) - \Phi_2(x_k, y)) \, \mathrm{d}s(y), \\ v_k = \quad & \frac{\partial u^i}{\partial n}(x_k) - \sum_{j=1}^{M} v_j \int_{\gamma_j} \left(\frac{\partial \Phi_1(x_k, y)}{\partial n(x)} - \frac{\partial \Phi(x_k, y)}{\partial n(x)} \right) \mathrm{d}s(y) \qquad (4.39) \\ & - \sum_{j=1}^{M} u_j \left(\frac{\partial}{\partial n} \int_{\gamma_j} \frac{\partial \Phi_2(x_k, y)}{\partial n(y)} \mathrm{d}s(y) \Big|_{x=x_k} - \frac{\partial}{\partial n} \int_{\gamma_j} \frac{\partial \Phi_1(x_k, y)}{\partial n(y)} \mathrm{d}s(y) \Big|_{x=x_k} \right). \end{aligned}$$

This generates a linear system of $2M$ simultaneous equations to determine the $2M$ unknowns $u_1, ..., u_M, v_1, ..., v_M$. This system can be written in the matrix form

$$\mathbf{U} = \mathbf{b} - B\mathbf{U}, \qquad (4.40)$$

where

$$\mathbf{U} = \begin{pmatrix} u_1 \\ \vdots \\ u_M \\ v_1 \\ \vdots \\ v_M \end{pmatrix}, \qquad (4.41)$$

and $\mathbf{b}$ is the column vector whose k^{th} entry is $u^i(x_k)$ for $k = 1, ...M$, and $\frac{\partial u^i}{\partial n}(x_k)$ for $k = M + 1, ..., 2M$. The kj^{th} entries of B are defined as

$$B_{kj} := \begin{cases} \int_{\gamma_j} \left(\frac{\partial \Phi_2(x_k, y)}{\partial n(y)} - \frac{\partial \Phi_1(x_k, y)}{\partial n(y)} \right) \mathrm{d}s(y), & \text{for } j = 1, ...M, \\ \int_{\gamma_j} (\Phi_2(x_k, y) - \Phi_1(x_k, y)) \, \mathrm{d}s(y), & \text{for } j = M + 1, ..., 2M, \end{cases}$$

if $1 \leq k \leq M$ and

$$B_{kj} = \begin{cases} \frac{\partial}{\partial n(x)} \int_{\gamma_j} \frac{\partial \Phi_1(x_j, y)}{\partial n(y)} \mathrm{d}s(y) - \frac{\partial}{\partial n(x)} \int_{\gamma_j} \frac{\partial \Phi_2(x_k, y)}{\partial n(y)} \mathrm{d}s(y), & \text{for } j = 1, ...M, \\ \int_{\gamma_j} \left(\frac{\partial \Phi_2(x_j, y)}{\partial n(y)} - \frac{\partial \Phi_1(x_k, y)}{\partial n(y)} \right) \mathrm{d}s(y), & \text{for } j = M + 1, ..., 2M, \end{cases}$$

if $M+1 \leq k \leq 2M$. We can rewrite (4.40) as

$$A\mathbf{U} = \mathbf{b}, \tag{4.42}$$

where

$$A := I + B.$$

After assembling our matrix A, the next step is to solve the matrix system (4.42) to obtain $\mathbf{U}$. We may then use Green's representation theorems (4.14) and (4.15) to calculate the field at any point in the domain.

The computational cost of this BEM scales with the size parameter X (which was defined in Chapter 1) since the mesh we use requires 10 elements per wavelength in order to capture the wave behaviour accurately. Hence it is easy to see that for large X the computational power required becomes too large for most machines. The output of using such a BEM can be seen in Figures 4.2(a) and 4.2(b). The BEM code used in this thesis is provided courtesy of David Hewett. Figure 4.2(a) shows the field u on the boundary of the shape. Equations (4.14) and (4.15) tell us that knowledge of u and $\frac{\partial u}{\partial n}$ on the boundary are sufficient to determine the field in $\mathbb{R}^2$, which is shown in Figure 4.2(b). In Figure 4.2(b) the diffraction effects can be seen propagating into the shape from the 4 corners which are first hit by the incident light. It is these effects which are not accounted for in the ray tracing method which we give a presentation of in the following chapter.

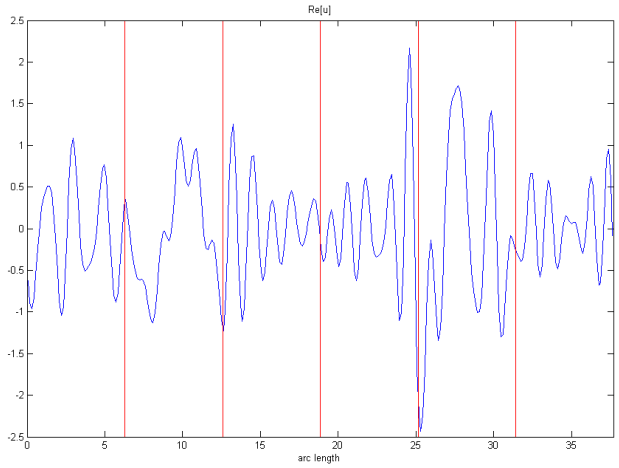

(a) Real part of u on boundary. The vertical red lines represent the corners of the hexagon, the first corner at 0 arc length is the one located at the top-right of the hexagon. Arc length increases as we go anti-clockwise around the boundary.

(b) Incident light with wavenumber $k = 5$ and amplitude $A = 1$ irradiates the hexagon from the top left. Plot shows the real part of u in the entire domain.

Figure 4.2: Plots showing the approximation to the field produced by the boundary element method.

Chapter 5

Ray Tracing Algorithm

In this chapter we apply the high frequency ray tracing method to obtain an approximation to the field on the boundary of the polygon.

When the incident plane wave strikes the ice crystal, it will be diffracted and reflected. The new directions of these diffracted and reflected beams will depend upon which side of the polygon the light has hit. Since we consider a plane wave which stretches to infinity in the directions perpendicular to its propagation, it will likely hit more than one side. In ray tracing we suppose each side which is 'illuminated' by the incident light gives rise to two beams, one reflected and one transmitted, travelling in new directions. The task of a ray tracing algorithm is to follow the transmitted beams as they travel around inside the shape and each time a beam strikes a side (see Figure 1.2), the RTA calculates the new transmitted and reflected beams along with their directions and amplitudes. The RTA then continues to track these new beams and so on ad infinitum.

Of course, it is not possible to perform these calculations for infinitely many reflections/transmissions so we must truncate the algorithm after a certain number of these reflections, call this number M. We may then evaluate the field on the boundary of the shape by summing the contributions from each of the beams. In Figure 5.1 the first

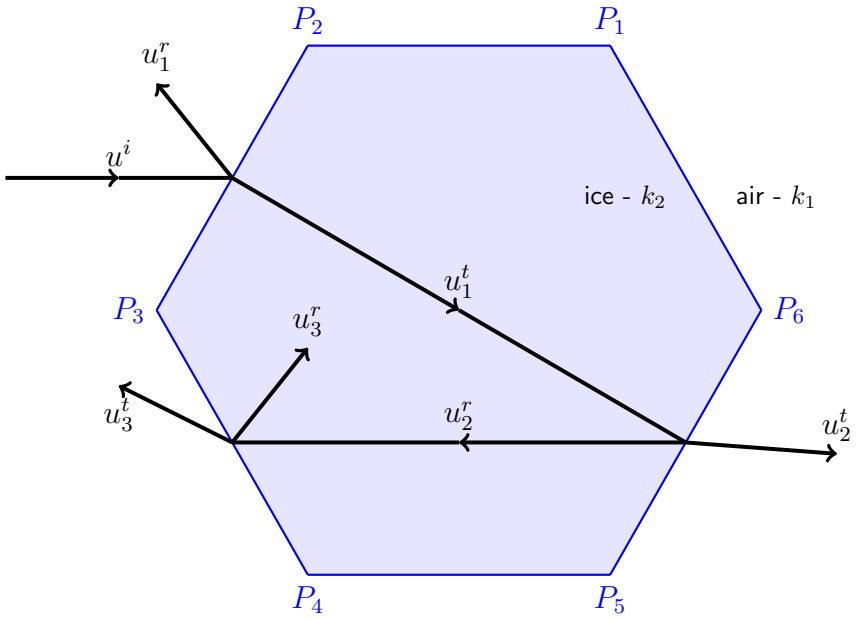

Figure 5.1: Ray tracing.

transmitted beam is denoted by u_1^t and subsequent transmitted beams which leave the shape are denoted u_j^t, for $j = 2, ..., M$. Similarly, the first reflected beam is u_1^r, the other reflected beams arise from the initial transmitted beam, these are written as u_j^r, for $j = 2, ..., M$. Therefore the field on the boundary, approaching from the interior is

$$u = u_1^t + \sum_{j=2}^{M} u_j^r + u_d, \tag{5.1}$$

where u_d is the field due to diffraction. Likewise, if we evaluate the field on the boundary, approaching from the exterior we find

$$u = u^i + u_1^r + \sum_{j=2}^{M} u_j^t + u_d. \tag{5.2}$$

These evaluations shall be elaborated upon in §5.3.

In this chapter we derive the necessary equations for designing a RTA. These equations include Snell's Law and the Fresnel equations, of which various derivations are known (e.g. see [9]). However, here we provide derivations of a more mathematical ilk

to many, and in a coordinate invariant form, which will be convenient for implementation. We note that a published reference including similar derivations is not known to the author. Later in the chapter, in §5.3, we discuss some of the results obtained from implementing the RTA and pose questions which are to be resolved in the following chapter. But first, let us begin with one of the most fundamental laws of optics.

5.1 Snell's Law

Snell's Law describes the relationship between the angles of incidence and transmission when light waves pass from one isotropic medium into another, in our case we are concerned with the two media air and ice. As can be seen in Figure 5.2 the angle of incidence θ_i is the angle measured anti-clockwise from the outward pointing normal $\hat{n}$ (directed out of the ice) to the direction vector of the incident light u^i. Similarly the angle of transmission θ_t is the angle measured anti-clockwise from the inward pointing normal to the direction vector of the transmitted light u^t. In addition to deriving Snell's law, we also must state the law of reflection which we quote from [9]. Hence we must also define the angle of reflection θ_r; this is the angle measured anti-clockwise from the direction vector of the reflected light u^r to the outward pointing normal.

To begin with we consider, for simplicity, a setup in which the boundary between ice and air passes through the origin of our general coordinates (x, y), more specifically we take our boundary to be $y = 0$. We also utilise the boundary conditions (4.3)–(4.4) which we restate for convenience,

$$[u] = 0, \qquad \left[\frac{\partial u}{\partial n}\right] = 0, \tag{5.3}$$

both on $y = 0$.

Now suppose a two-dimensional incident plane wave u^i with direction $\mathbf{d}^i$ strikes the boundary $y = 0$. Part of this light is reflected with direction $\mathbf{d}^r$ and the remainder is

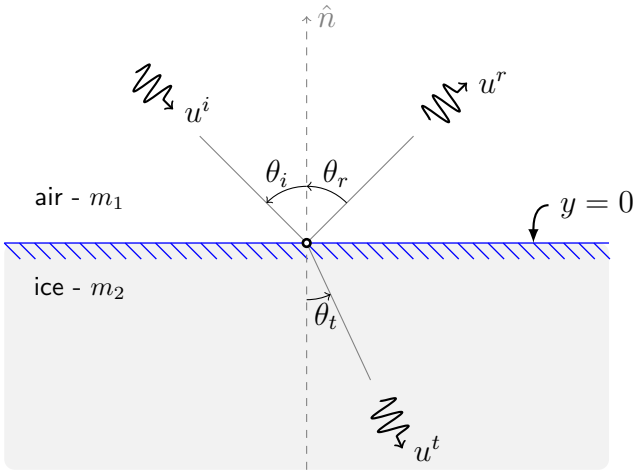

Figure 5.2: Refraction and reflection of light at the interface $y = 0$

transmitted with direction $\mathbf{d}^t$. The *law of reflection* [9] states that

$$\theta_r = \theta_i, \tag{5.4}$$

and so we may write these direction vectors in the following form

$$\mathbf{d}^i = (\sin\theta_i, -\cos\theta_i), \quad \mathbf{d}^r = (\sin\theta_i, \cos\theta_i), \quad \mathbf{d}^t = (\sin\theta_t, -\cos\theta_t). \tag{5.5}$$

The general form of a plane wave is $u = Ae^{ik\mathbf{x}\cdot\mathbf{d}}$ where A is the amplitude, $\mathbf{x}$ the position, k the wavenumber and $\mathbf{d}$ the direction vector of the wave. So, using (5.5), the incident plane wave may be written as

$$u^i = A^i e^{ik_1(x\sin\theta_i - y\sin\theta_i)}, \tag{5.6}$$

where A^i is the amplitude and the wave propagates in the half-plane $y > 0$. The total field in $y > 0$ in this scenario is $u = u^i + u^r$ where

$$u^r = A^r e^{ik_1(x\sin\theta_i + y\sin\theta_i)}, \tag{5.7}$$

is the reflected wave. In the half-plane $y < 0$ the total field is $u = u^t$ where the transmitted wave is

$$u^t = A^t e^{ik_2(x\sin\theta_t - y\sin\theta_t)}. \tag{5.8}$$

Here k_1 and k_2 represent the wavenumbers of the wave in air and ice respectively, and are related by

$$\frac{k_1}{k_2} = \frac{m_1}{m_2} = \frac{c_2}{c_1}, \tag{5.9}$$

where m_1 and m_2 are the refractive indices of air and ice as stated previously and c_1 and c_2 are the wavespeeds of light in these two media, respectively. The relationships between the amplitudes A^i, A^r and A^t will be derived later in §5.2 and §5.2.1.

We now consider the the first of the boundary conditions (5.3); this implies that

$$u^i + u^r = u^t. \tag{5.10}$$

Substituting for the u's using (5.6)–(5.8) and noting that $y = 0$ on the boundary we have

$$A^i \mathrm{e}^{\mathrm{i}k_1 x \sin\theta_i} + A^r \mathrm{e}^{\mathrm{i}k_1 x \sin\theta_i} = A^t \mathrm{e}^{\mathrm{i}k_2 x \sin\theta_t}, \tag{5.11}$$

and rearranging finally gives

$$\frac{A^i + A^r}{A^t} \mathrm{e}^{\mathrm{i}x(k_1 \sin\theta_i - k_2 \sin\theta_t)} = 1. \tag{5.12}$$

Equation (5.12) must hold for all $x \in \mathbb{C}$, which implies *Snell's Law of Refraction*

$$k_1 \sin\theta_i - k_2 \sin\theta_t = 0. \tag{5.13}$$

This also implies that the amplitudes are related by

$$A^i + A^r = A^t. \tag{5.14}$$

5.1.1 Snell's Law in vector form

We have derived Snell's Law for the case when the boundary at $y = 0$ as in Figure 5.2. However, in our polygon in Figure 5.1 each side represents a boundary in a different position and orientation. In order to cope with a boundary in any position or orientation it is necessary to find expressions for $\mathbf{d}^i, \mathbf{d}^r$ and $\mathbf{d}^t$ which are not explicitly dependent

upon the angles θ_i, θ_r and θ_t. This is because each time we are on a new boundary, the normal to that boundary will be different from the normal to the previous one, which means that we must define a new way to measure these angles each time. In this subsection we demonstrate how to find these new expressions.

The expressions in (5.5) show how the directions $\mathbf{d}^i$, $\mathbf{d}^r$ and $\mathbf{d}^t$ can be written in terms of the incident and transmitted angles when we take the interface to be $y = 0$. In this particular example, we may decompose the incident direction vector, say, into x- and y- components respectively as

$$\begin{aligned} \mathbf{d}^i &= (\sin\theta_i, -\cos\theta_i) \\ &= \underbrace{(\sin\theta_i, 0)}_{x\text{-component}} + \underbrace{(0, -\cos\theta_i)}_{y\text{-component}}. \end{aligned}$$

For a general vector, $\mathbf{d}$, we may do a similar operation but this time decompose components which are tangential and normal to the boundary,

$$\mathbf{d} = \underbrace{\mathbf{d} - (\mathbf{d}\cdot\mathbf{n})\mathbf{n}}_{\text{tangential component}} + \underbrace{(\mathbf{d}\cdot\mathbf{n})\mathbf{n}}_{\text{normal component}} \tag{5.15}$$

Using (5.15) and Snell's Law (5.13), $\mathbf{d}^t$ can be written as

$$\begin{aligned} \mathbf{d}^t &= (\sin\theta_t, 0) + (0, -\cos\theta_t) \\ &= \frac{k_1}{k_2}(\sin\theta_i, 0) + \left(0, -\sqrt{1 - \left(\frac{k_1}{k_2}\sin\theta_t\right)^2}\right) \\ &= \frac{k_1}{k_2}\left(\mathbf{d}^i - (\mathbf{d}^i\cdot\mathbf{n})\mathbf{n}\right) - \frac{k_1}{k_2}\left[\left(\frac{k_2}{k_1}\right)^2 - 1 + \cos^2\theta_i\right]^{\frac{1}{2}}\mathbf{n}, \end{aligned}$$

which, after replacing $\cos\theta_i$ with $\mathbf{d}^i\cdot\mathbf{n}$, becomes

$$\mathbf{d}^t = \frac{k_1}{k_2}\left\{\mathbf{d}^i - (\mathbf{d}^i\cdot\mathbf{n})\mathbf{n} - \left[\left(\frac{k_2}{k_1}\right)^2 - 1 + (\mathbf{d}^i\cdot\mathbf{n})^2\right]^{\frac{1}{2}}\right\}\mathbf{n}. \tag{5.16}$$

Similarly, the expression for the reflected direction is found to be

$$\mathbf{d}^r = \mathbf{d}^i - 2(\mathbf{d}^i\cdot\mathbf{n})\mathbf{n}. \tag{5.17}$$

5.2 Fresnel Equations

In section 5.1 we found one relationship between the 3 quantities A^i, A^r and A^t, namely equation (5.14). The Fresnel equations provide two more relations between these amplitudes which allow us to determine their values. Here we will derive the Fresnel equations, firstly in the setup described in section 5.1, in which the interface between the two media is the line $y = 0$ (as in [10]), and secondly in a more general setup.

Writing the second of the boundary conditions (5.3) using the plane wave form $u = A\mathrm{e}^{\mathrm{i}k\mathbf{x}\cdot\mathbf{d}}$ and using (5.10), we have

$$-\mathrm{i}k_1 \cos\theta_i u^i + \mathrm{i}k_1 \cos\theta_i u^r = -\mathrm{i}k_2 \cos\theta_t (u^i + u^r),$$

which after cancellation and rearrangement becomes

$$u^r = \frac{k_1 \cos\theta_i - k_2 \cos\theta_t}{k_1 \cos\theta_i + k_2 \cos\theta_t} u^i. \tag{5.18}$$

Now, on $y = 0$, $u^r = A^r \mathrm{e}^{\mathrm{i}k_1 x \sin\theta_i}$ and $u^i = A^i \mathrm{e}^{\mathrm{i}k_1 x \sin\theta_i}$ so from (5.18) we obtain an expression for the reflection coefficient which is the first of the Fresnel equations,

$$R := \frac{A^r}{A^i} = \frac{\cos\theta_i - \alpha(\theta_i)}{\cos\theta_i + \alpha(\theta_i)}, \tag{5.19}$$

where

$$\alpha(\theta_i) = \frac{1}{\zeta}\sqrt{1 - \zeta^2 \sin^2\theta_i}, \tag{5.20}$$

in which

$$\zeta := \frac{k_1}{k_2}, \tag{5.21}$$

is the relative refractive index. Notice that when $1/\zeta > 1$ (which is the case when the light travels from the air into the ice, in fact here $1/\zeta = 1.31$) and $\theta_i < \arcsin(1/\zeta)$, α is real and positive. This implies that $|R| < 1$ and so the amplitude of the reflected wave is smaller that the amplitude of the incident wave. Also, by Snell's Law (5.13), $\theta_t < \theta_i$, so the effect of refraction is to 'bend' the light towards the normal to the boundary, a physical phenomenon which was explained in §3.3 using a more intuitive (but less rigorous) argument.

However, when $1/\zeta < 1$ (i.e. when the light travels back out of the ice crystal into the air, here $1/\zeta = 0.76$) it is possible for α to be imaginary. In fact, α is imaginary when the incident angle θ_i exceeds the *critical angle* $\theta_c = \arcsin(1/\zeta)$. In this case $|R| = 1$ and the amplitude of the transmitted wave is equal to that of the incident wave. There is still a transmitted wave, however it is exponentially decaying as $y \to -\infty$ [10]. This phenomenon is known as *total internal reflection*. This name is useful as it tells us that it only occurs on the interior of the ice crystal.

Now we derive the second of the Fresnel equations. From (5.14) we know that

$$1 + \frac{A^r}{A^i} = \frac{A^t}{A^i}, \tag{5.22}$$

or rather

$$1 + R = T, \tag{5.23}$$

where $T := A^t/A^i$ is the transmission coefficient. Hence the second of the Fresnel equations is

$$T = \frac{2\cos\theta_i}{\cos\theta_i + \alpha(\theta_i)}. \tag{5.24}$$

It can easily be shown that the vector form of the Fresnel equations is

$$R = \frac{\mathbf{d}^i \cdot \mathbf{n} - \alpha}{\mathbf{d}^i \cdot \mathbf{n} + \alpha}, \tag{5.25}$$

$$T = \frac{2\mathbf{d}^i \cdot \mathbf{n}}{\mathbf{d}^i \cdot \mathbf{n} + \alpha}, \tag{5.26}$$

where

$$\alpha = \frac{1}{\zeta}\sqrt{1 - \zeta^2 + \zeta^2 \mathbf{d}^i \cdot \mathbf{n}}. \tag{5.27}$$

5.2.1 Generalised Fresnel Equations

The Fresnel equations stated in the previous section were derived under the assumption that one of the coordinate axes coincides with the interface. When tracking light beams around the interior of the polygon and considering the interaction of the beams with each of the different sides, it is desirable to have a form of the Fresnel equations which is

in terms of a single coordinate system but relevant for interfaces that lie away from the origin of this system and are not aligned with these coordinate directions as illustrated in Figure 5.3.

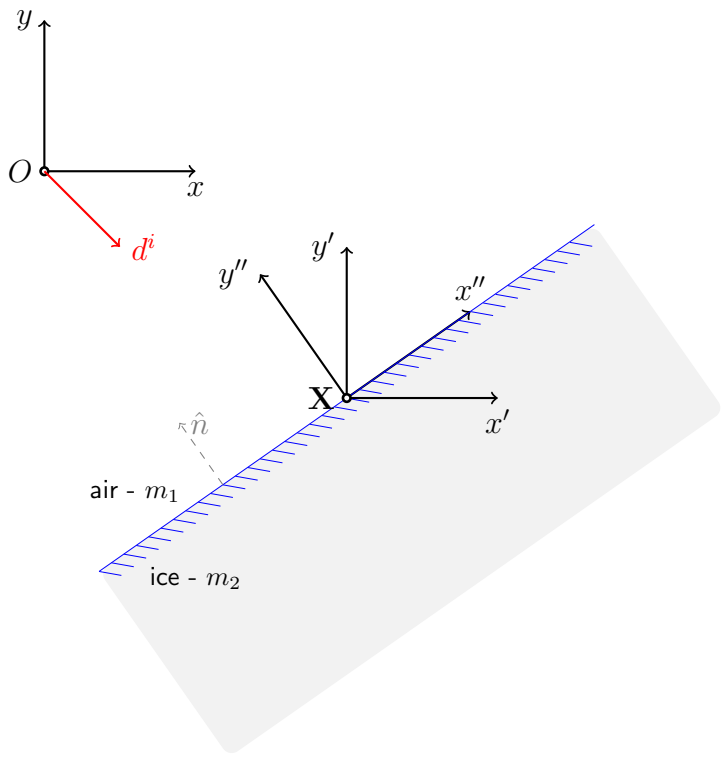

Figure 5.3: Coordinate shift and rotation.

Suppose $\mathbf{X}$ is a point on the interface and O is the origin of the general coordinate system. The coordinate system (x, y) is our general system and the coordinates (x'', y'') are equivalent to those used in Figure 5.2 since they are in the plane of the interface. To transform from (x, y)– to (x', y')–coordinates we simply shift by $\mathbf{X}$,

$$\mathbf{x}' = \mathbf{x} - \mathbf{X}. \tag{5.28}$$

Then in order to transform from (x', y')– to (x'', y'')–coordinates we rotate using a rotation matrix M,

$$\mathbf{x}'' = M\mathbf{x}', \tag{5.29}$$

where M is orthogonal, i.e. it satisfies $M^{\mathrm{T}}M = MM^{\mathrm{T}} = 1$. So, combining (5.28) and (5.29) we obtain

$$\mathbf{x}'' = M(\mathbf{x} - \mathbf{X}), \tag{5.30}$$

which is the transformation from (x, y)- to (x'', y'')-coordinates.

Let us begin by rewriting the representations of the incident, reflected and transmitted rays (5.6)–(5.8) in vector form as

$$u^i = A^i \exp\left\{\mathrm{i}k_1 \mathbf{d}^i \cdot \mathbf{x}\right\}, \tag{5.31}$$

$$u^r = A^r \exp\left\{\mathrm{i}k_1 \mathbf{d}^r \cdot \mathbf{x}\right\}, \tag{5.32}$$

$$u^t = A^t \exp\left\{\mathrm{i}k_2 \mathbf{d}^t \cdot \mathbf{x}\right\}. \tag{5.33}$$

In order to derive the desired Fresnel equations we must transform (5.31)–(5.33) into (x'', y'')-coordinates, solve the problem as in §5.2, then transform back into general coordinates. In (x'', y'')-coordinates we have

$$u^i = \left(A^i\right)'' \exp\left\{\mathrm{i}k_1 (\mathbf{d}^i)'' \cdot \mathbf{x}''\right\}, \tag{5.34}$$

$$u^r = (A^r)'' \exp\left\{\mathrm{i}k_1 (\mathbf{d}^r)'' \cdot \mathbf{x}''\right\}, \tag{5.35}$$

$$u^t = \left(A^t\right)'' \exp\left\{ik_2 (\mathbf{d}^t)'' \cdot \mathbf{x}''\right\}, \tag{5.36}$$

where $\mathbf{x}'' = M(\mathbf{x} - X)$, $(\mathbf{d}^i)'' = M^{-1}\mathbf{d}^i$ and $\left(A^i\right)''$ etc. are to be determined. Starting with (5.34) and expanding gives

$$\begin{aligned} u^i &= \left(A^i\right)'' \exp\left\{\mathrm{i}k_1 \left(M^{-1}\mathbf{d}^i\right) \cdot (M(\mathbf{x} - \mathbf{X}))\right\} \\ &= \left(A^i\right)'' \exp\left\{\mathrm{i}k_1 \mathbf{d}^i \cdot (\mathbf{x} - \mathbf{X})\right\} \\ &= \left(A^i\right)'' \exp\left\{-\mathrm{i}k_1 \mathbf{d}^i \cdot \mathbf{X}\right\} \exp\left\{\mathrm{i}k_1 \mathbf{d}^i \cdot \mathbf{x}\right\}. \end{aligned} \tag{5.37}$$

Similarly for the reflected and transmitted waves we have

$$u^r = (A^r)'' \exp\left\{-\mathrm{i}k_1 \mathbf{d}^r \cdot \mathbf{X}\right\} \exp\left\{\mathrm{i}k_1 \mathbf{d}^r \cdot \mathbf{x}\right\} \tag{5.38}$$

and

$$u^t = \left(A^t\right)'' \exp\left\{-\mathrm{i}k_2 \mathbf{d}^t \cdot \mathbf{X}\right\} \exp\left\{\mathrm{i}k_2 \mathbf{d}^t \cdot \mathbf{x}\right\}. \tag{5.39}$$

By comparing (5.37)–(5.39) with (5.31)–(5.33) we notice that

$$A^i = \left(A^i\right)'' \exp\left\{-\mathrm{i}k_1 \mathbf{d}^i \cdot \mathbf{X}\right\}, \tag{5.40}$$

$$A^r = (A^r)'' \exp\left\{-\mathrm{i}k_1 \mathbf{d}^r \cdot \mathbf{X}\right\}, \tag{5.41}$$

$$A^t = \left(A^t\right)'' \exp\left\{-\mathrm{i}k_2 \mathbf{d}^t \cdot \mathbf{X}\right\}. \tag{5.42}$$

The reflection coefficient R in general coordinates is defined as the ratio of the reflected amplitude to the incident amplitude, so we may now write

$$R := \frac{A^r}{A^i} = \frac{(A^r)'' \exp\left\{-\mathrm{i}k_1 \mathbf{d}^r \cdot \mathbf{X}\right\}}{(A^i)'' \exp\left\{-\mathrm{i}k_1 \mathbf{d}^i \cdot \mathbf{X}\right\}}. \tag{5.43}$$

Writing $R'' := (A^r)''/(A^i)''$ and $\mathbf{d}^r = \mathbf{d}^i - 2(\mathbf{d}^i \cdot \mathbf{n})\mathbf{n}$ using (5.17), we obtain after cancellation

$$R = R'' \exp\left\{2\mathrm{i}k_1 (\mathbf{d}^i \cdot \mathbf{n})(\mathbf{n} \cdot X)\right\}, \tag{5.44}$$

where R'' is the reflection coefficient on the boundary $y'' = 0$ which is calculated as in (5.25). The term multiplying R'' in (5.44) represents a phase shift due to the offsetting of the origin from the interface. Using the same method but for $T'' := (A^t)''/(A^i)''$ yields

$$T := \frac{A^t}{A^i} = T'' \exp\left\{-ik_1 \left[(\mathbf{d}^i \cdot \mathbf{n}) - \mathrm{sgn}(\mathbf{d}^i \cdot \mathbf{n}) \left(\left(\frac{k_2}{k_1}\right)^2 - 1 + (\mathbf{d}^i \cdot \mathbf{n})^2\right)^{1/2}\right] (\mathbf{n} \cdot X)\right\}. \tag{5.45}$$

Note the $\mathrm{sgn}(\mathbf{d}^i \cdot \mathbf{n})$ which has been included so that the expression is valid on the interior of the shape also, since here the normal directions to the sides are reversed. It is important to note that the equations derived in this chapter are valid for the scenario when light is propagating *into* the ice crystal, i.e. from air to ice. In order to make them valid for the scenario when light is propagating *out of* the ice crystal, all we need to do is switch the refractive indices k_1 and k_2. This is easily implemented in the algorithm since the first scenario mentioned is relevant only for the inital wave transmission/reflection, that is when u^i his the crystal and splits into u_1^r and u_1^t in Figure 5.1.

5.3 Evaluating the boundary data

As an example, we consider a square crystal illuminated from the top left, as in Figure 5.5. The incident plane wave will strike sides Γ_1 and Γ_2 of the crystal, giving rise to a transmitted and reflected beam from each. Figure 5.4 shows the transmitted beam from Γ_1 and the reflected beam it causes once it strikes Γ_4, this beam will strike sides Γ_2 and Γ_3 giving rise to more beams and so on. The formulae derived in §5.1 and §5.2 govern the directions of these reflected and transmitted beams, and the amplitudes of their associated fields. So once these formulae are programmed in the form of a RTA code and run on a computer for M reflections/transmissions, we will build up a large array of data which gives us the details of: the number of beams which have hit each side, their widths and positions, and their transmitted and reflected directions and amplitudes.

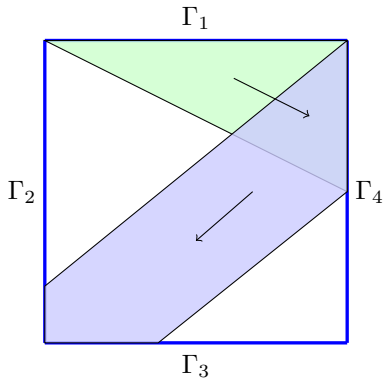

Figure 5.4: Ray tracing inside the polygon. Note that the transmitted rays have not been included in this diagram.

In order to evaluate the contribution to the electric field of each of these beams, we use the formula

$$u(\mathbf{x}) = A\mathrm{e}^{\mathrm{i}k\mathbf{d}\cdot\mathbf{x}}. \tag{5.46}$$

However, as was alluded to in the introduction to this chapter, we have an array of

beams bouncing around inside the crystal, and also an array of beams transmitted out of the crystal, so which do we choose when evaluating the field? Due to the boundary condition $[u] = 0$, either may be chosen so long as we remain consistent.

So, (using the notation from Figure 5.1) summing the beams in the interior leads to the ray tracing approximation for the boundary field (or leading order behaviour u_l) as

$$u_l = u_1^t + \sum_{j=2}^{M} u_j^r. \tag{5.47}$$

Whereas if we sum the beams which are propagate away from the shape, we have

$$u_l = u^i + u_1^r + \sum_{j=2}^{M} u_j^t, \tag{5.48}$$

where u_j^t and u_j^r are calculated using the formulae (5.35)–(5.36) derived in §5.2.1. We choose the first option (5.47) in our implementation. Note that (5.47)–(5.48) differ from (5.1)–(5.2) in that the first two do not include u_d. This is because (5.47) and (5.48) are the fields given by the RTA, which does not account for diffraction, so the fields will have no u_d term.

Now let us look at some outputs from our implementation of the RTA. Consider the setup illustrated in Figure 5.5 in which a square ice crystal with refractive index $m_2 = 1.31$ is irradiated from the top left by a plane wave with wavenumber $k = 5$ and amplitude $A = 1$. The length of each side is 2π so that 5 wavelengths of light fit along each side, this also ensures that the size parameter X is equal to k. The origin of the coordinate system is located at the centre of the square. Figure 5.6 shows the real and imaginary parts of u around the boundary for $M = 50$. The vertical red lines depict the corners of the square going anti-clockwise from $\theta = 0$, which we choose as P_1. So the first red line represents P_2, the second P_3, etc. Note that the field on the first two sides, Γ_1 and Γ_2, are symmetrical, as are the fields on the final two, Γ_3 and Γ_4. This is a consequence of the origin's location at the centre of the shape and the 45° incident angle of the light. If we were to shift the origin or alter the incident light's direction, this symmetry would be lost. We also notice that the field is larger on Γ_3 and Γ_4, which

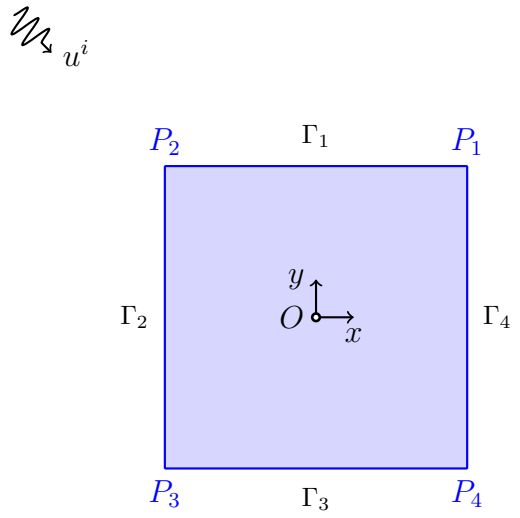

Figure 5.5: Setup for the square with $P_1 = (\pi, \pi)$, $P_2 = (-\pi, \pi)$, $P_3 = (-\pi, -\pi)$ and $P_4 = (\pi, -\pi)$.

suggests that more light is transmitted through the shape than is reflected away from the illuminated sides Γ_1 and Γ_2. This is intuitive because we know from experience that ice is transparent. If we were to make the refractive index of the scatterer very large, the reverse would be true. Increasing the refractive index is equivalent to making the scatterer more opaque.

Figure 5.7 shows how the field changes after each reflection/transmission. The first plot shows the field on the boundary after only Γ_1 and Γ_2 have been illuminated by the incident light. The second plot shows the field after the light has passed into the top left of the square and out of the bottom right, which at first thought might seem to be enough tracking of the ray as to give a good representation of the field. However from looking at the later plots, it is evident that the contributions from subsequent internal reflections have a significant effect on the total field on the boundary (although the contributions diminish with each reflection as we shall see in the next chapter).

An interesting question arises here: *How many internal reflections, M, is it necessary to track in order to obtain an accurate representation of the field on the boundary?*

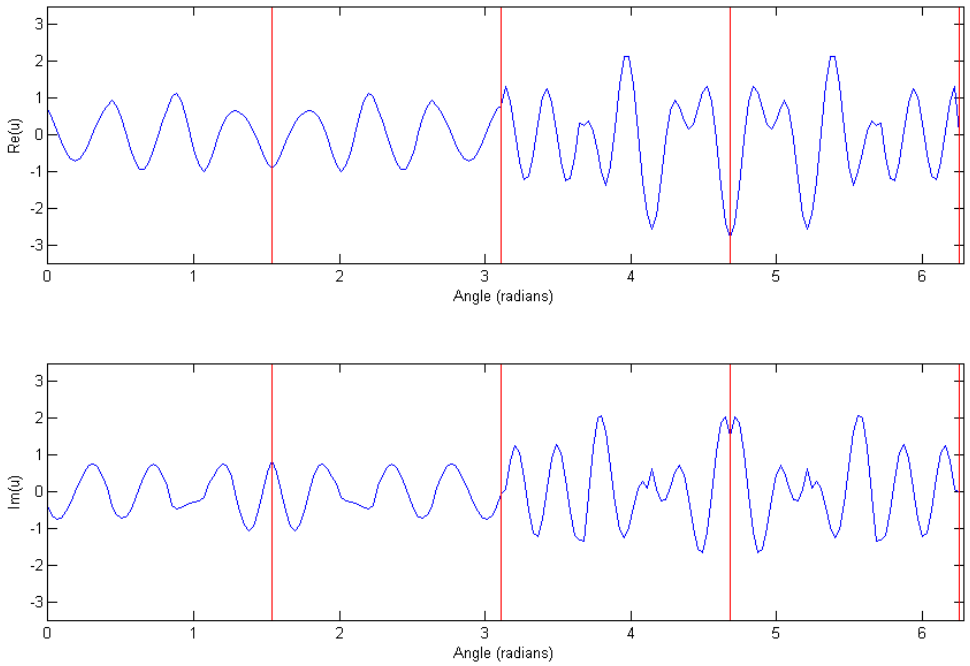

Figure 5.6: Ray tracing approximation with $M = 50$ of the electric field on the boundary of the square ice crystal in Figure 5.5 which is being irradiated by light with wavenumber $k = 5$, amplitude $A = 1$ and direction $\mathbf{d}^i = (1, -1)$.

If we can determine this, then we may use the answer to truncate the number of reflections the algorithm calculates, hence saving on computing time. Other questions stem from this, such as *How does M depend on the wavenumber, the amplitude or the shape of the obstacle?*.

Once we ascertain M, we may make fair comparisons between the fields generated by the RTA and BEM. Recall that the RTA does not incorporate diffraction, whereas the BEM does. So by comparing the outputs of these two methods we may be able to isolate the effects of diffraction. Questions we hope to answer are *What form do diffraction effects take?* and *Is there a precise formula that captures the behaviour of diffraction in the transmission problem?* These questions, and those of the preceeding

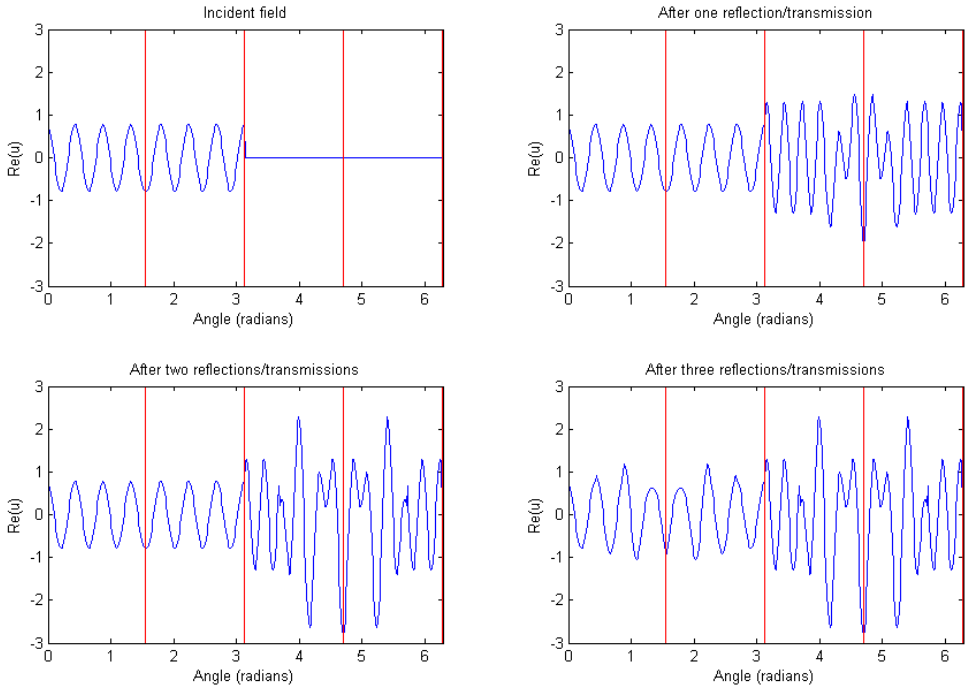

Figure 5.7: Ray tracing approximation of the electric field on the boundary of the square crystal in Figure 5.5 which is being irradiated by light with wavenumber $k = 5$, amplitude $A = 1$ and direction $\mathbf{d}^i = (1, -1)$. Each subsequent plot shows the field after considering one more reflection/transmission, so we go from $M = 1$ to $M = 4$.

paragraph, are discussed in the following chapter.

Chapter 6

Results and Discussion

This chapter discusses the questions posed at the conclusion of the previous chapter, in an attempt to better understand the behaviour of diffraction (the term u_d) in our problem. We first wish to ascertain how many reflections/transmissions (M) to consider in the RTA to obtain an accurate description of the leading order component of the scattered field. This issue is dealt with in §6.1.

Once the answer to this question has been established we may proceed to §6.2 where we subtract the leading order behaviour obtained by ray tracing, from the approximation obtained using the BEM, in order to establish the importance, and study the influence, of diffraction.

6.1 Convergence of solution

This section discusses the question *How many internal reflections, M, is it necessary to track in order to obtain an accurate representation of the field on the boundary?* Which is another way of asking: How quickly does the ray tracing approximation converge?

In order to analyse this convergence, we will take the field on the boundary after

50 reflections ($M = 50$) as the 'exact' solution[1], U, and will evaluate the Euclidean or l^2-norm of the difference between the exact solution and the solution after M reflections for $M = 1, 2, ..., 49$, i.e.

$$error_M = \left(\sum_{i=1}^{L} |u_i - U_i|^2 \right)^{1/2}, \quad \text{for } M = 1, ..., 49, \tag{6.1}$$

where L is the number of grid points around the boundary at which u is calculated.

Figure 6.1(a) shows a logarithmic plot of $error_M$ against M for the scenario in Figure 5.5 with varying k. Straight lines on a log plot imply that the convergence to the exact solution is exponential, in fact, for the square the equation of the line is roughly

$$error_M = \underbrace{2.8}_{\alpha} \exp\{\underbrace{-0.92}_{\beta} M\}. \tag{6.2}$$

It is of note that the figure suggests that β is independent of k. Also it is worth mentioning that the slight divergence of the lines after $M = 40$ can be ignored since at this point the error is 10^{-16} which is machine precision, so we may assume that the data after this point is unreliable. This would imply that, in order to obtain machine precision with the RTA, we may take $M = 40$ as sufficient.

We remark that this rate of convergence is specific to the relative refractive index of ice to air, i.e. 1.31. If we increase the refractive index of ice, to 2 for example, we can expect a much slower convergence as is verified by Figure 6.2. We see here that the RTA requires $M = 60$ to reach machine precision. This is because for a higher refractive index, the incidence of total internal reflection is more common. Why total internal reflection is important to the convergence of the ray tracing algorithm shall be studied in the following subsection.

[1]In this section we use the word 'solution' to refer to the ray tracing approximation, and the phrase 'exact solution' as shorthand for the ray tracing approximation for $M = 50$.

6.1.1 Exponential convergence and geometric series

The exponential convergence of the ray tracing method to the exact solution can be explained by comparing the series of reflected beams to a geometric series. As the bundle of light beams are reflected around inside the shape, the amplitude of each reflected beam is smaller than its preceeding one by a factor of R (where R is the reflection coefficient) unless total internal reflection occurs. A series in which successive terms share a common ratio is a *geometric series*, i.e. a series of the form

$$a + ar + ar^2 + ar^3 + ..., \tag{6.3}$$

where r is the common ratio.

For a ray travelling around inside the square of ice with incident light directed at 45° to the illuminated sides (as in Figure 5.5), the ray will undergo either total internal reflection or reflection with coefficient $R = 0.2186$. If we ignore total internal reflection and phase shift, the geometric series for the amplitude of this ray is

$$A + AR + AR^2 + ... + AR^{M-1} = A\frac{1 - R^M}{1 - R}, \tag{6.4}$$

where A is the amplitude of the incident light. The sum of the infinite series is $A/(1-R)$, so the error incurred by truncating after M reflections is

$$\frac{A}{1 - R} - A\frac{1 - R^M}{1 - R} = \frac{AR^M}{1 - R}. \tag{6.5}$$

Plotting this alongside the RT error decay (see Figure 6.3) shows us that the convergence of the geometric series is faster. But this is probably due to ignoring total internal reflection in which $|R| = 1$. Although the convergence plots do not match, the qualitative comparison is instructive.

Indeed, formula (6.5) suggests that the rate of convergence is dependent on R, so if R is usually small, then the solution should converge quickly and if it is usually large, the solution should converge more slowly. This equates to saying that the obstacle shape and the angle of the incident light have an effect on the rate at which $error_M \to 0$.

We might expect that shapes with more sides will cause a slower rate of convergence since the angles of incidence (recall this angle is measured from the normal to each side as in Figure 5.2) within the shape are more likely to be large, and hence there is a greater chance of total internal reflection and R in general will be large. Figure 6.1(b) demonstrates how this rate varies for different shapes. Note that the regularly spaced kinks are due to total internal reflection.

Although we have seen that (6.5) is not a true representation of $error_M$, it can be seen as a lower bound on this error. Also it can be used to determine roughly how much faster or slower one particular setup will converge compared to another. By setup, it is meant the combination of incident light angle and obstacle shape. For example, one need only perform a few calculations 'by hand' using the Fresnel formula (5.19) for the two setups to find a common or 'characterstic' value of R for each, input this value into (6.5) and compare the results.

Formula (6.5) also suggests that the rate of convergence should be independent of the wavenumber, which is consistent with the results shown in Figure 6.1(a). This result demonstrates that ray tracing is a frequency independent method and so is considerably more efficient than the BEM for high frequencies.

6.2 Ray Tracing vs. BEM

The main objective of this thesis is to examine the difference, u_d, between the exact solution[2] u and the leading order behaviour u_l and in this section we do exactly this. The BEM takes into account the diffraction of light from the corners of the obstacle, which is a physical feature that is not picked up using our ray tracing technique. So we expect some difference between the two solutions. Figure 6.4(a) shows u calculated using the two different methods. The setup is again as shown in Figure 5.5, i.e. a square

[2]In this section we return to the original use of the term 'solution', i.e. the exact solution refers to the solution of the scattering problem

crystal being illuminated from the top left. The angle θ in Figure 6.4(a) is measured in radians anti-clockwise from the first corner P_1, at which $\theta = 0$. The corner which is first hit by the incident light is P_2 which is located at $\theta = \pi$ rad in Figure 6.4(a) (also shown by the first vertical red line from the left). We notice good agreement on the illuminated sides Γ_1 and Γ_2 between the two approximations as well as at P_4, however along the shadow sides, Γ_3 and Γ_4, the agreement is considerably weaker which suggests that the diffraction effects are large on the sides in shadow as well as on the shadow side of corners P_1 and P_3.

Figure 6.4(b) shows u_d alone. This plot better identifies the regions which have been affected most by the effects of diffraction from the corners of the square. The regions of large u_d are on sides Γ_3 and Γ_4 which is to be expected since the diffracted light is propagating from the corners in the top left through the shape towards the bottom right. For this particular scenario, with $k = 10$, u_d is fairly uniform over these two sides, this is because diffraction effects are large for a low wavenumber such as this, so they will spread out over a wide region. It would be instructive to look to higher frequencies, where the diffracted regions are narrower, in order to seek a pattern. But how do we know which frequencies are good to use for this purpose? In order to answer this, we choose some measure of the difference between the two approximated fields and analyse its behaviour as k increases. We do this in the next subsection and return in §6.2.2, better informed, to the task of ascertaining the effect of diffraction on the field around the boundary.

6.2.1 Relative Error

As the frequency of the incident light is increased, the effects of diffraction diminish and so we expect the outputs from the BEM and RT to become more similar. By considering the relative error between the two solutions it is possible to see precisely how the two solutions converge as k increases. The definition of this relative error, E

is as follows

$$E := \frac{||u_{BEM} - u_{RT}||}{||u_{BEM}||} \approx \frac{||u - u_l||}{||u||}, \tag{6.6}$$

where $||.||$ is the l^2-norm, defined as in (6.1). The number of points L (see (6.1)) used in this norm is chosen as the number of elements at which the approximations are calculated in the two methods. The BEM uses 10 elements per wavelength along each side of the square in order to retain resolution of the waves. So, for example, $L = 800$ for the square with side length 2π and incident wavenumber $k = 20$. We run the RTA at the same resolution as the BEM to give a fair comparison.

This error measures how close the leading order behaviour of u is to the exact value of u. We would expect that for high frequencies (large k), E is small, since ray tracing techniques are more accurate for large values of the crystal size parameter, as was discussed in Chapter 2. As can be seen from Table 6.1 this is indeed the case. The values in the table approximately follow the trend given by the equation

$$E = 0.34k^{-0.57}, \tag{6.7}$$

which was calculated using Excel's curve-fitting tool. So we see that the BEM approximation is approaching the RT approximation as k is increased, however the rate at which the two converge decreases as k increases. Therefore, the two approximations will never match perfectly. This is in accordance with the fact that the 'shadow boundaries' in Figure 6.6 become narrower as the incident light's frequency is increased and our ray tracing approximation is an asymptotic method, to which reality converges as $k \to \infty$. We also note from the table that the relative error ranges from 14% for $k = 5$ down to 4.2% for $k = 40$ which strongly suggests how the accuracy of our ray tracing method is limited to very high wavenumbers. If, for example, we seek to use ray tracing to obtain an approximation which is accurate to within 1%, we can use (6.7) to calculate that we require the wavenumber of the incident light to be approximately 27600.

For many applications an accuracy of 5% may be sufficient in which case the RTA presented here is a tremendously efficient technique. However, considering our appli-

Wavenumber (k)	Relative error(E)
5	1.4×10^{-1}
10	8.8×10^{-2}
15	7.0×10^{-2}
20	6.7×10^{-2}
25	5.3×10^{-2}
30	5.0×10^{-2}
35	4.4×10^{-2}
40	4.2×10^{-2}

Table 6.1: Table of relative error between BEM and RT methods

cation to clouds which contain potentially millions of ice crystals, we desire our error to be smaller since this error may become compounded once scattered light hits another crystal which further scatters the light which goes on to hit another crystal etc. It is also evident that we have no control over the accuracy of the RTA for a fixed wavenumber. Whereas we do for a BEM, since we may increase the number of degrees of freedom in order to do so. This is a desirable feature to have and provides a great amount of flexibility for a method. For these reasons we can confirm that our aim to develop a computationally feasible and accurate method for a large range of values of the size parameter X is substantiated.

We now return to analysing the regions of the field on the boundary where diffraction has its greatest effects. This is done most easily by looking at plots of u_d. Also, considering the results in Table 6.1 it appears that studying wavenumbers greater than $k = 30$ will enable us to see the effects of diffraction more clearly.

6.2.2 Diffraction

Figure 6.5 shows u_d round the boundary of the square for incident light of wavenumber $k = 30$. A pattern in which the high values are grouped is beginning to appear, most notably at four distinct regions along each of the sides Γ_3 and Γ_4. We highlight these regions on Γ_3 alone (since the patterns on Γ_3 and Γ_4 are symmetrical) in the field's imaginary component for $k = 30$ in Figure 6.5. They are approximately located in the ranges $\theta = 3.14$ to 3.2, $\theta = 3.6$ to 3.8, $\theta = 4.$ to 4.25 and $\theta = 4.3$ to 4.4. If we consider how the diffraction at the corners travels around within the shape as in Figure 6.6 we can explain these areas of large difference between the leading order and exact solutions.

Figure 6.6 shows a schematic representation of some of the effects of diffraction by the corners of the crystal. The three corners which are illuminated by the incident wave diffract the light and generate 'shadow boundaries' which surround the edges of the beam predicted by ray tracing. We see in schematic (b) of this figure that after the shadow boundaries are reflected once, there are four regions on each of the sides Γ_3 and Γ_4 which are affected by diffraction. Comparing these regions to those in Figure 6.5 which we highlighted above, there is a convincing match. This result implies that, in theory, if one could calculate the nature, i.e. shape and size, of these shadow boundaries, then we could input this data into the RTA and predict where they would travel to.

One issue stands in the way of this approach however, and it is that, as remarked in Chaper 1, no exact solution for the diffraction by a 2D penetrable wedge (corner) is currently known. However, further studies of the width and intensity of these regions in u_d may help us to infer the exact form this diffusion takes and hence the precise form of the shadow boundaries. But we leave such in-detail scrutiny of u_d to future work. For the mean time, we may attempt to conjecture the form this diffraction takes. We first will briefly consider the diffraction behaviour for the sound-soft (non-transmission case).

In the sound-soft case, Chandler-Wilde and Langdon [6] demonstrated that diffraction by corners leads to waves of the form

$$u_d(s) = \frac{\mathrm{i}}{2}\left(\mathrm{e}^{\mathrm{i}ks}v^+(s) + \mathrm{e}^{\mathrm{i}ks}v^-(s)\right), \tag{6.8}$$

which propagate along the sides of the polygon. In equation (6.8), s is the arc-length along the side, k is the wavenumber and $v^{\pm}$ are integral equations which are detailed in [6], p624. In [17], Silveira assumes that diffraction in the transmission problem takes the same form as (6.8) and arrives at results which do not substatiate this assumption.

We would expect that the precise influence of diffraction in this transmission problem is some blend of waves propagating down the sides of the polygon and waves propagating through the obstacle, as depicted in Figure 6.6. The formula (6.8) leads us to conjecture that the diffracted waves propagating through the obstacle have the form

$$u_d(r) = e^{\mathrm{i}kr}V(r), \tag{6.9}$$

where r is the radial distance from the corner and $V(r)$ is some unknown funtion which may be determined in future work. Equation (6.9) is an educated guess for the diffraction from one corner, so if we want to model a polygon with n vertices, a possible form is

$$u_d(\mathbf{x}) = \sum_{j=1}^{n} e^{\mathrm{i}k\mathbf{x}}V_j(\mathbf{x}), \tag{6.10}$$

where $\mathbf{x}$ is a point on the interior of the polygon. For the time being these are conjectures, and they serve to conclude the main body of work in this thesis.

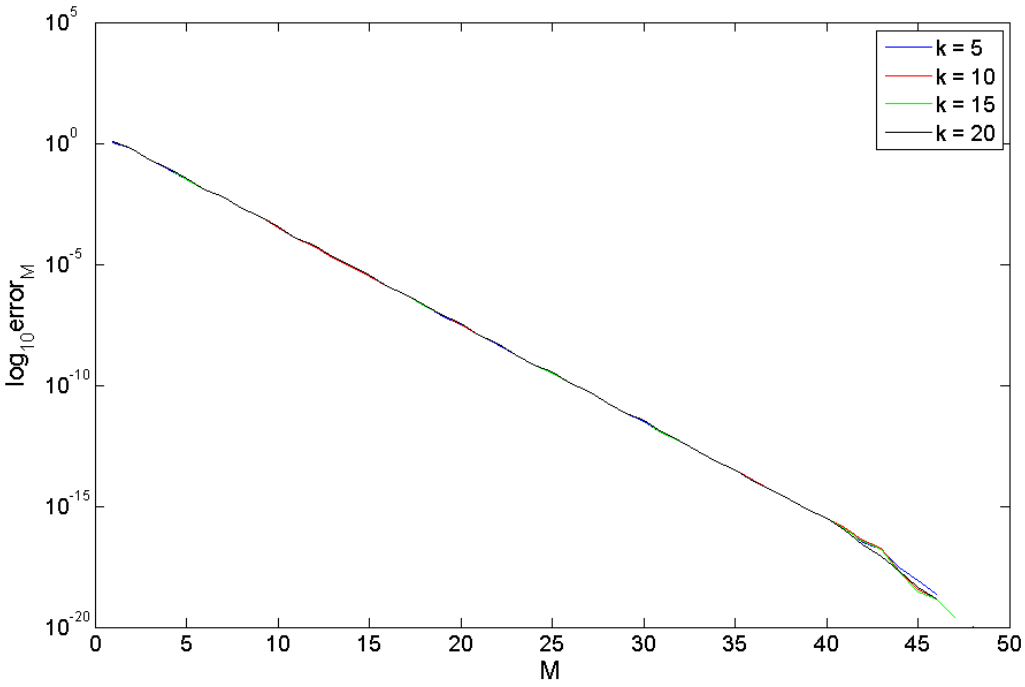

(a) Decay of $error_M$ for the square with varying wavenumber k.

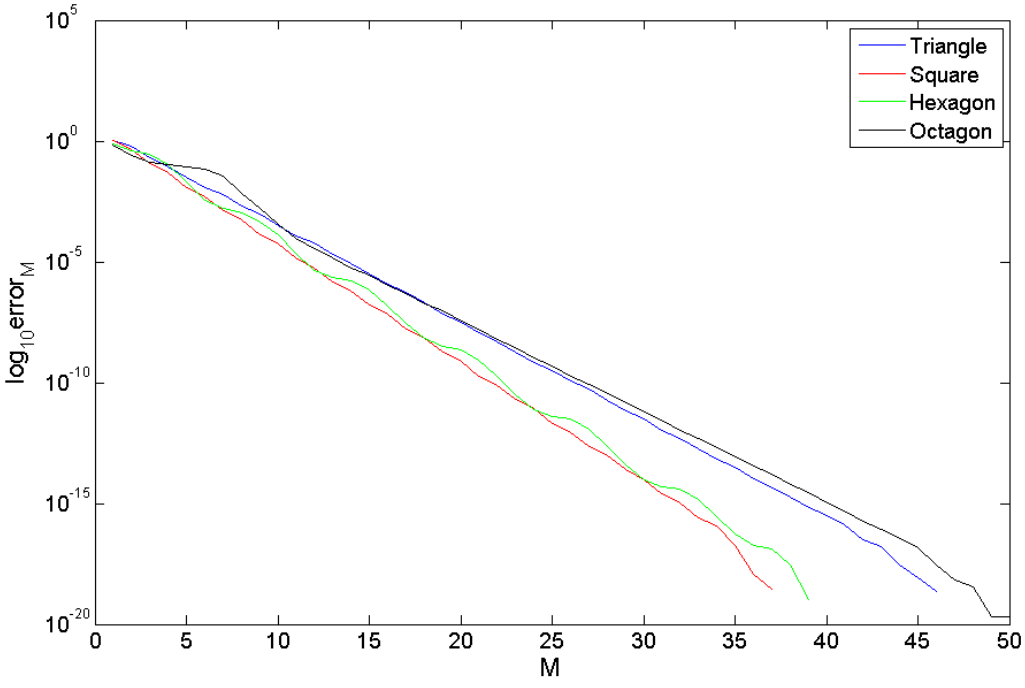

(b) Decay of $error_M$ for scatterers of different shapes and wavenumber $k = 10$.

Figure 6.1: Plots showing the logarithm of $error_M$ against the number of reflections/transmissions M.

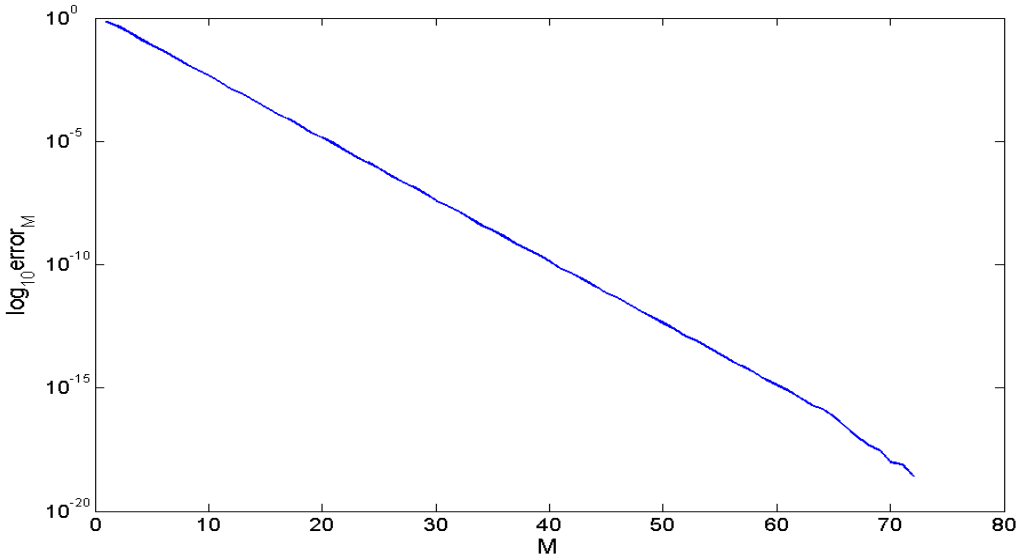

Figure 6.2: Decay of $error_M$ for square obstacle with refractive index $m_2 = 2$ and incident light wavenumber $k = 10$.

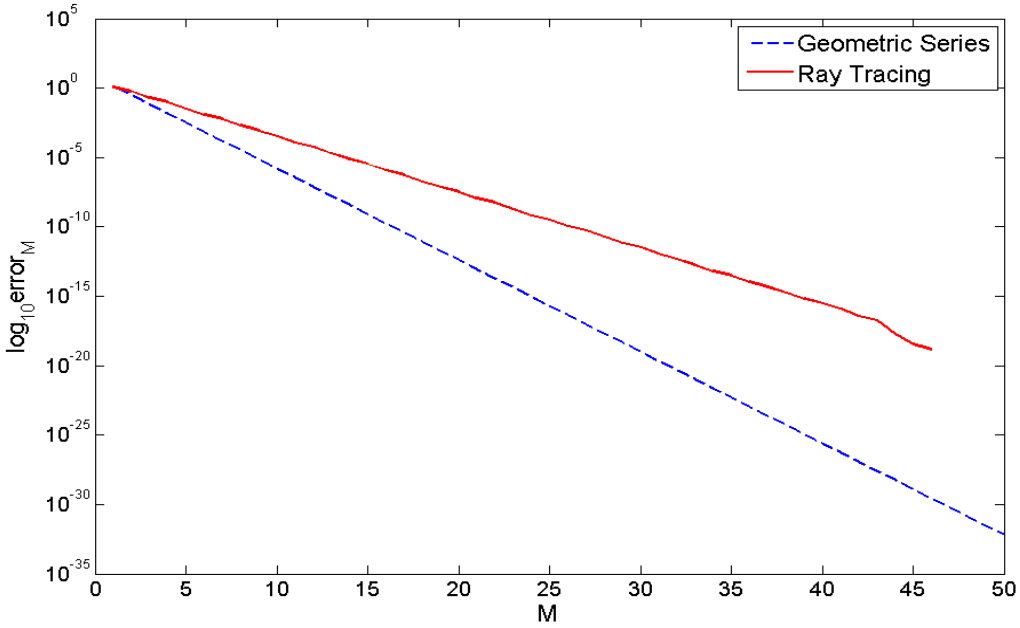

Figure 6.3: Error decay of geometric series versus error decay of RT

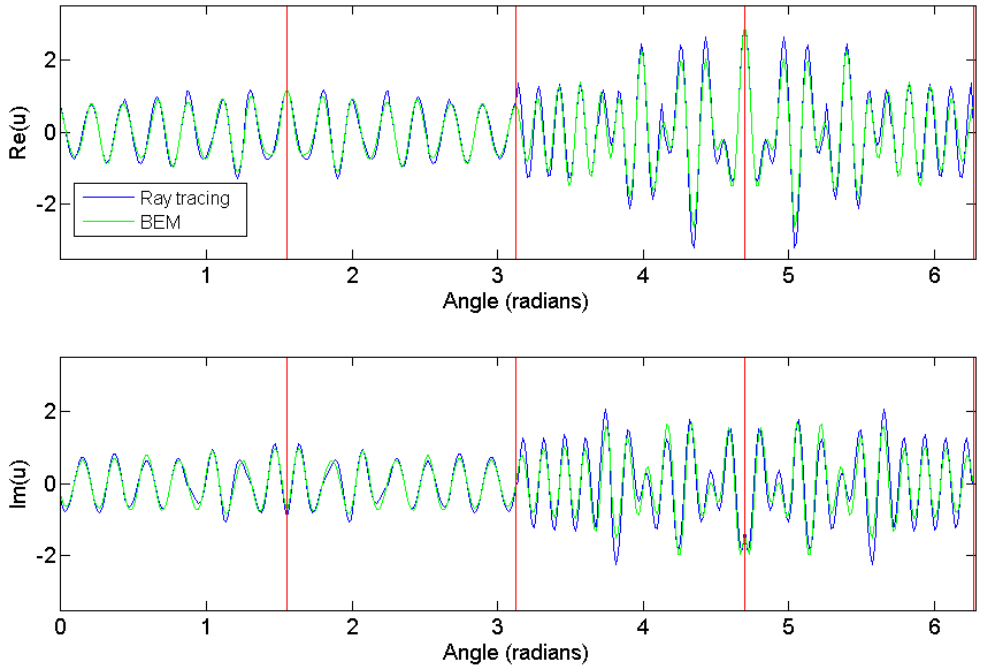

(a) Comparison of u on boundary calculated using BEM and RTA.

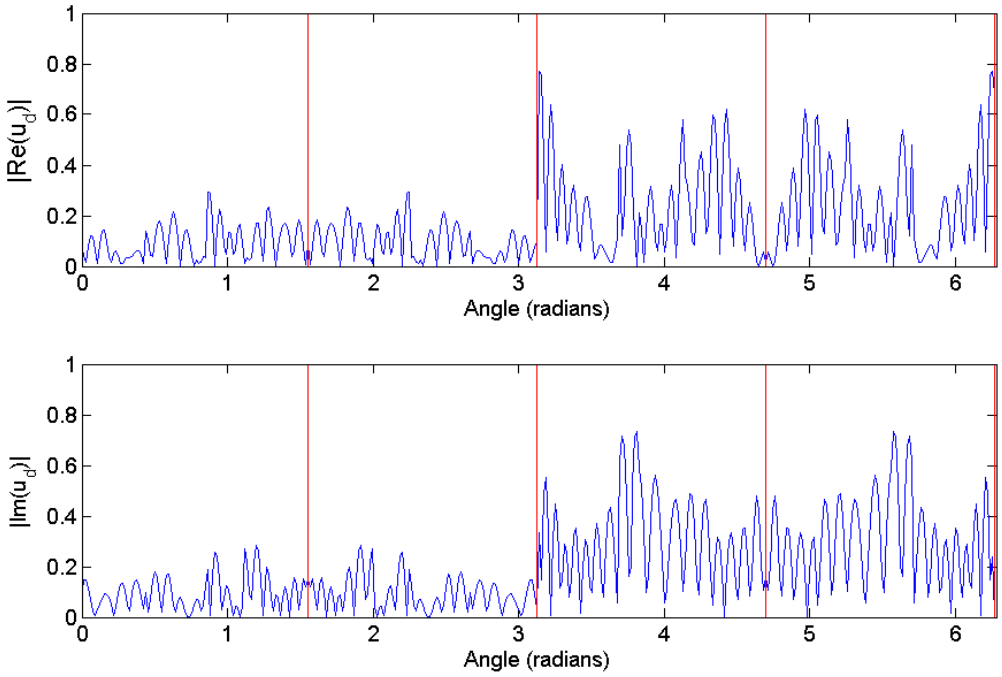

(b) Absolute values of the real and imaginary components of u_d on the boundary.

Figure 6.4: Comparisons between outputs of BEM and RTA for square scatterer irradiated by light with wavenumber $k = 10$.

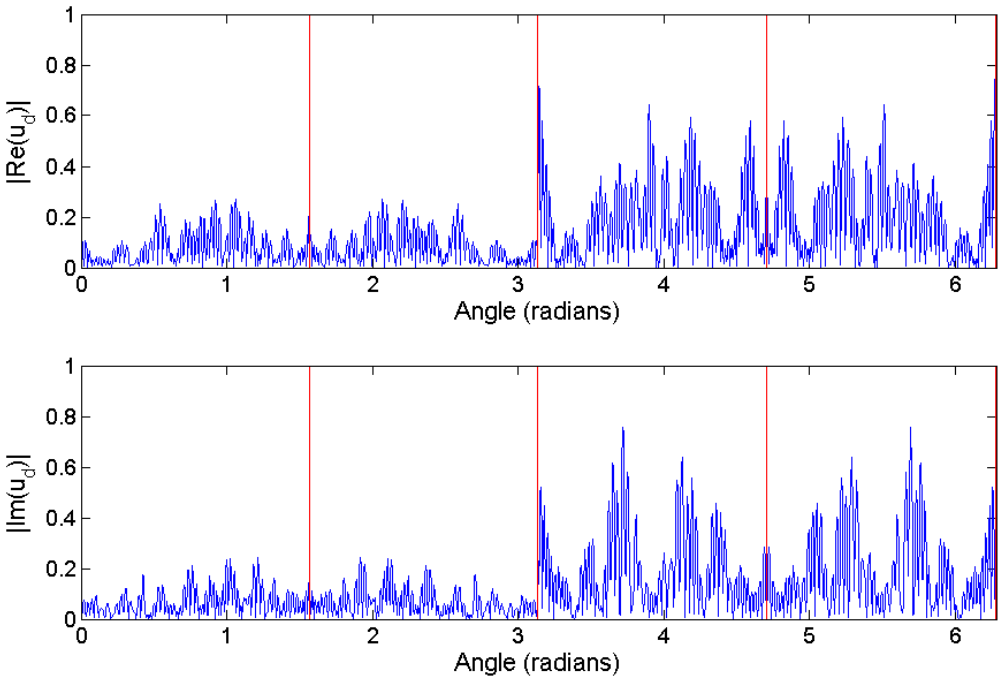

Figure 6.5: Absolute values of the real and imaginary components of u_d on the boundary of the square with incident light of wavenumber $k = 30$.

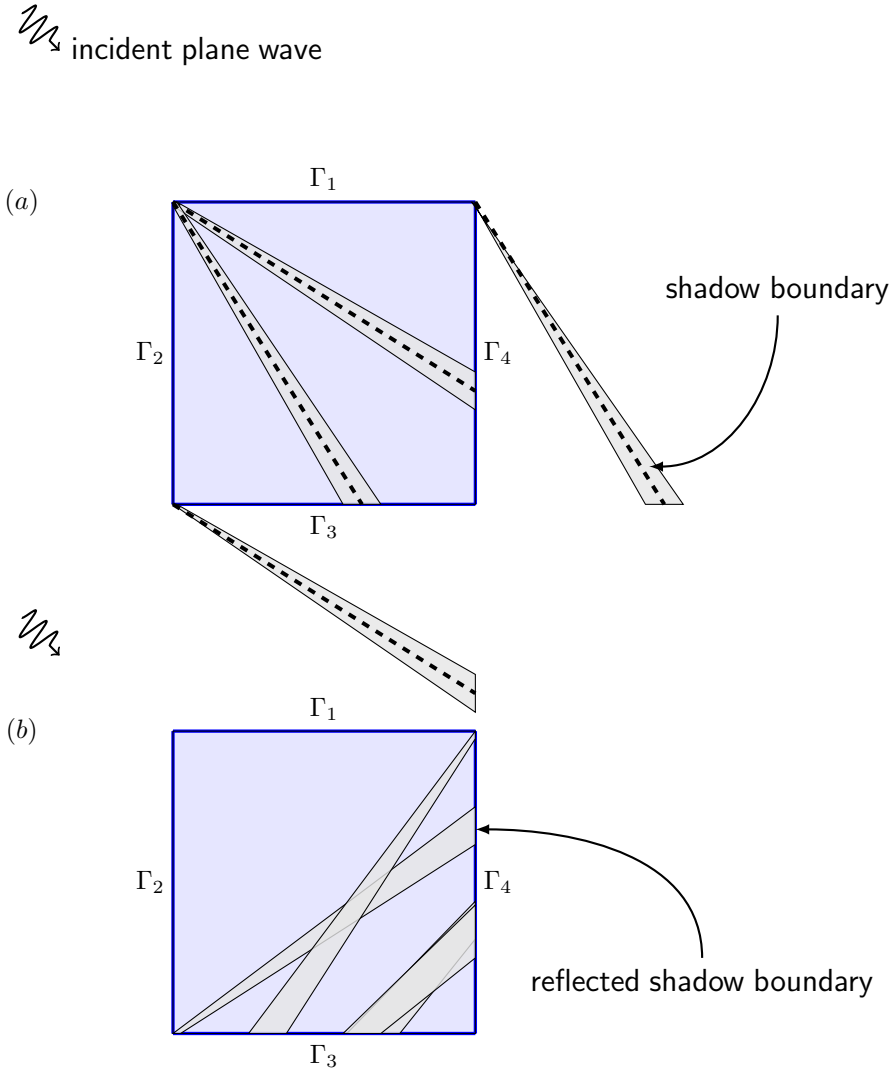

Figure 6.6: How diffracted fields are reflected within the shape. The dashed lines represent the beam edges as predicted by ray theory.

Chapter 7

Conclusions and Future Work

This study has attempted the challenging task of ascertaining the behaviour of time-harmonic wave scattering by a two-dimensional penetrable obstacle. In this final chapter, we provide a summary of the work done in this thesis in order to achieve this aim, and also detail the conclusions we have made. We finish in §7.2 by discussing some ideas for possible future progress in modelling the transmission problem.

7.1 Summary and Conclusion

In the opening chapters of this thesis, we introduced the problem of time-harmonic light scattering in two-dimensions. An important application of this work to atmospheric science was discussed, namely determining the light scattering properties of cirrus clouds, which in turn leads to consequences for climate prediction. Then a brief review of some of the literature on the subject was conducted. We established that at present there exists a void in the range of ice crystal size parameters for which the light scattering properties can be modelled accurately or efficiently. Either side of the void sit separate groups of methods, namely numerical methods for small X and geometrical optics methods for large X.

We set out to design and implement a geometrical optics approach and compare the output to that of a numerical method with the ambitious goal of understanding the effect of diffraction in the transmission problem. Once these effects are understood, we may exploit this knowledge to design a numerical method to apply to crystals with size parameters which lie in the void.

In Chapter 3, Maxwell's equations were stated along with the appropriate boundary conditions and it was shown that the problem of time-harmonic light scattering in two dimensions is equivalent to the much studied acoustic transmission problem. In Chapter 4 the problem was stated mathematically in the form we wished to solve. Then, using Green's representation theorems, we reformulated the problem as an integral equation on the boundary of the scatterer. A standard BEM for the problem was also shown. This BEM is highly accurate but suffers from a computational cost that grows at least linearly with the size parameter X.

In Chapter 5 we set out the equations required for ray tracing. In particular, we derived coordinate invariant formulae for the direction vectors of reflected and transmitted rays, with the aid of Snell's Law, which was also proved. Also we provided a derivation of the coordinate invariant Fresnel equations which give us the reflection and transmission coefficients. These formulae together constitute the mathematics required for writing a ray tracing algorithm.

The ray tracing algorithm was implemented in Chapter 6 in order to approximate the leading-order behaviour of the scattered field. In the first half of this chapter it was established that, for the case of the square crystal, the approximation produced by the RTA settles down after roughly 40 reflections/tranmissions and we gave a mathematical justification of this using geometric series. This result enabled us to make a fair comparison between the approximations produced by the RTA and BEM in the second half of this chapter. This geometric series approximation also demonstrated that the RTA is frequency (or X) independent.

By considering the relative error between the approximations obtained using the RTA and the BEM, we showed that diffraction effects are substantial in the transmission problem and hence an asymptotic approach, such as the ray tracing method employed here, is not sufficiently accurate (within 1%) for frequencies which are not large. Moreover, the error incurred in using our ray tracing algorithm is not 'controllable'. This is because the error is not due to the coarseness of the grid used or poor approximating polynomials, but is caused by the initial assumption that we may ignore diffraction effects.

Although a poor method if one requires high accuracy at low or medium frequencies, the RTA is a useful tool for obtaining the leading order behaviour of the scattered field. It does this very efficiently, indeed we have shown that the computational cost of the RTA is frequency independent. Using the RTA to approximate the leading order behaviour, and using a boundary element method to obtain the total field, we examined the difference which we supposed was due to diffraction.

Analysing the field due to diffraction, u_d, we found a simple explanation for why some regions of the field are affected more than others. We explained that the effect of diffraction is to create shadow boundaries around the beam edges as in Figure 6.6. Where ray tracing predicts a discontinuity, i.e. light one side of the beam edge and none the other side, diffraction acts to blur these boundaries. So we have that diffracted light hits part of a side which ray tracing predicted would not be hit. Once we understand this basic idea, then we may track the shadow boundaries as they reflect around the shape in 'ray tracing' style.

We concluded the results chapter by making two conjectures as to a basic form for diffraction in the transmission problem, inspired by the sound-soft form of Chadler-Wilde and Langdon [6]. These conjectured forms may prove to be crude guesses since it is likely that there is a ray-tracing component to be considered. However, we leave any such probing to future work.

7.2 Further Work

There is a great deal of work to be done before an X-independent numerical method for this transmission problem is developed and the 'gap' mentioned in Chapter 2 is bridged. In order to achieve this, we must obtain a better understanding of diffraction through penetrable obstacles. To reach such an understanding, further experimentation with the RTA and BEM would prove beneficial. In particular, it would be instructive to examine how u_d changes as the angle of the incident light is altered. It would also be worthwhile considering in detail obstacles of different shapes.

In this thesis, we studied the square crystal in most detail. This was done for clarity of presentation since the expected symmetry was identifiable and, using the same shape throughout, it was easier to draw reliable conclusions about the convergence and diffraction patterns. However, in order to gather data about the diffraction of penetrable corners, studying the triangle would be more helpful since it is the shape most like a single wedge. In fact, to better isolate diffraction, considering the infinite penetrable wedge as in [16] (see Figure 7.1), would be useful.

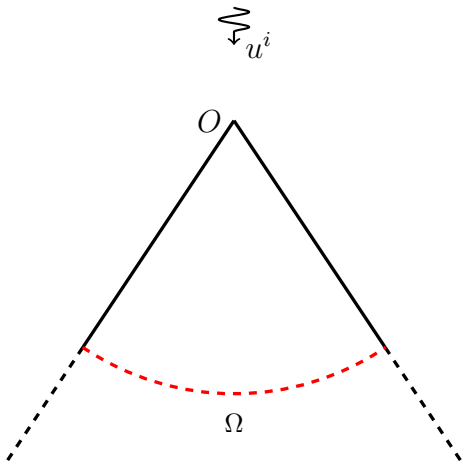

Figure 7.1: Diffraction by an infinite penetrable wedge.

Although this is moving away from ice crystal shapes (since it is not a polygon), I

believe this would be the best way to establish the form of diffraction, as conjectured in (6.9). We could again use the RTA and BEM to identify u_d on Ω in Figure 7.1. Here Ω is an imaginary line which is an arc of the circle centred at O. In order to do this, the BEM and RTA may have to be adapted slightly and perhaps it may prove better to employ a FEM instead of a BEM. To avoid adaptation of the codes one could also consider a very large triangle as an approximation to the open wedge.

Another feature of this problem to investigate would be the effect of diffraction on the 'far-field pattern', i.e. the field some distance away from the scatterer as opposed to the boundary data. It may even be noticed that the influence of diffraction is negligible in the far-field, although I believe this to be unlikely. A study may show that the behaviour of u_d in the far-field is easier to model or it may provide some insight into the issues discussed in this thesis, such as the functional form (6.9). Also, considering the application to light scattering by cirrus cloud, it is the far-field that we are interested in ascertaining so why not study this from the outset? Of course, there are some very good reasons for studying the effects on the boundary, such as Green's representation theorems. However, it may prove a faster, although perhaps less elegant, route to understanding the scattering properties of cirrus clouds, to develop a theory for the approximate far-field behaviour which may be implemented soon.

Evidently, there is a large scope for possible future work on the transmission problem, not only in furthering the numerical approximation of the solution but also searching for the analytic solution to the problem of transmission through a penetrable wedge. Naturally, a discovery of the latter would aid the progress of the former.

Bibliography

[1] *Digital Library of Mathematical Functions*. National Institute of Standards and Technology, from http://dlmf.nist.gov/, release date: 2010-05-07.

[2] A. J. Baran, *A review of the light scattering properties of cirrus*, Journal of Quantitative Spectroscopy and Radiative Transfer, 110 (2009), pp. 1239–1260.

[3] A. J. Baran and L. C. Labonnote, *A self-consistent scattering model for cirrus. I: The solar region*, Q. J. R. Meteorol. Soc., 133 (2007), pp. 1899–1912.

[4] M. Born and E. Wolf, *Principles of Optics*, Cambridge University Press, 1997.

[5] S. N. Chandler-Wilde and S. Langdon, *Boundary element methods for acoustics*, July 2007. Lecture notes.

[6] ——, *A Galerkin boundary element method for high frequency scattering by convex polygons*, SIAM J. Numer. Anal., 45 (2007), pp. 610–640.

[7] D. Colton and R. Kress, *Integral Equation Methods in Scattering Theory*, Wiley, 1983.

[8] M. Costabel and E. Stephan, *A direct boundary integral equation method for transmission problems*, Journal of Mathematical Analysis and Applications, 106 (1985), pp. 367–413.

[9] E. Hecht, *Optics, 4th Edition*, Addison Wesley, 2002.

[10] D. Hewett, *Introduction to acoustics*, January 2011. Lecture notes.

[11] A. J. Heymsfield, K. M. Miller, and J. D. Sphinhirne, *The 27–28 October 1986 FIRE IFO cirrus case study: cloud microstructure*, Monthly Weather Review, 118 (1990), pp. 2313–2328.

[12] G. C. Hsiao and H. Liwei, *A system of boundary integral equations for the transmission problem in acoustics*, Applied Numerical Mathematics, 61 (2011), pp. 1017–1029.

[13] J. B. Keller, *Geometrical theory of diffraction*, Journal of the Optical Society of America, 52 (1996), pp. 116–130.

[14] W. McLean, *Strongly Elliptic Systems and Boundary Integral Equations*, Cambridge University Press, 2000.

[15] E. Perrey-Debain, O. Laghrouche, P. Bettess, and J. Trevelyan, *Plane-wave basis finite elements and boundary elements for three-dimensional wave scattering*, Phil. Trans. R. Soc. Lond. A, 362 (2004), pp. 561–577.

[16] A. D. Rawlins, *Diffraction by, or diffusion into, a penetrable wedge*, Proc. R. Soc. Lond. A, 455 (1999).

[17] R. Silveira, *Electromagnetic scattering by simple ice crystal shapes*, M.Sc. Thesis, University of Reading, (2006).

[18] P. Yang and K. N. Liou, *Light scattering by hexagonal ice crystals: comparison of finite-difference time domain and geometric optics models*, J. Opt. Soc. Am., 12 (1995), pp. 162–176.

[19] ——, *Geometric-optics-integral-equations method for light scattering by nonspherical ice crystals*, Applied Optics, 35 (1996), pp. 6568–6584.